AIAA AVIATION Forum
12-16 June 2023, San Diego, CA and Online
AIAA AVIATION 2023 Forum

10.2514/6.2023-4134

Surface Pressure Measurements and Predictions in Shock-Dominated Flows

Kirk R. Brouwer *
ARCTOS Technology Solutions, Beavercreek, OH, 45432, USA

Ricardo A. Perez †, Timothy J. Beberniss †, and S. Michael Spottswood ‡
Air Force Research Laboratory, Wright-Patterson AFB, OH, 45433, USA

Experiments on a rigid panel were conducted to characterize the mean and unsteady pressure fields beneath a shock/boundary layer interaction (SBLI) produced by an incident oblique shock in the Air Force Research Laboratory (AFRL) Research Cell 19 (RC-19) facility. Attached and separated SBLI conditions were considered. The effect of shock sweep on the loading environment was also investigated for an attached SBLI condition. A commercially available, fast, porous pressure sensitive paint (PSP) was used to obtain full-field, non-contact pressure measurements. Traditional, discrete pressure transducers were also used to evaluate the PSP measurements. The PSP was calibrated *in-situ* using images obtained at constant pressures during evacuation of the test section as well as pressure tap measurements from each run. Reynolds-averaged Navier-Stokes (RANS) analyses were conducted and compared with the time-averaged pressure fields. The time-averaged results demonstrate that the RANS solutions adequately reproduce the highly three-dimensional, SBLI-induced surface pressure loads. In regard to the unsteady pressure, the PSP captures the shock-induced peak in the root mean square pressure and the low-frequency shock oscillations associated with separated SBLI, while also providing a detailed, simultaneous global view of the three-dimensional interaction which is not easily obtained with traditional pressure transducers.

Downloaded by AFRL D'Azzo Wright-Patterson on July 13, 2023 | http://arc.aiaa.org | DOI: 10.2514/6.2023-4134

Nomenclature

$A(T), B(T), C(T)$	=	Temperature dependent Stern-Volmer terms
ESP	=	Electronically scanned pressure
f	=	Frequency
f_{NL}	=	Nonlinear regression model
G	=	Signal power
H	=	Height
h	=	Thickness
I	=	Image intensity
L	=	Length
M	=	Mach number
N	=	Vector length
$NRMSE$	=	Normalized root mean square error
p	=	Pressure
q	=	Dynamic pressure
Re	=	Reynolds number
RMS	=	Root mean square
r^2	=	Correlation coefficient
SST	=	Menter $k-\omega$ shear stress transport turbulence model

*Associate Research Engineer
†Research Aerospace Engineer, Aerospace Systems Directorate
‡Principal Aerospace Engineer, Aerospace Systems Directorate

Distribution Statement A: Approved for Public Release; Distribution is Unlimited; PA# AFRL-2023-1840; Cleared 04/18/2023.

This material is declared a work of the U.S. Government and is not subject to copyright protection in the United States.

St	=	Strouhal number
T	=	Temperature
U	=	Velocity
W	=	Width
$WKW06$	=	Wilcox (2006) $k-\omega$ turbulence model
x, y, z	=	Spatial coordinates
x_{Imp}	=	Shock impingement location
β	=	Shock sweep angle
Δx_{Wedge}	=	Streamwise distance from the wedge to panel leading edge
δ_{TBL}	=	Turbulent boundary layer thickness
θ	=	Flow turn angle
σ	=	RMS pressure

Subscripts

0	=	Total condition
∞	=	Freestream
i	=	Index
PSP	=	Pressure sensitive paint
p	=	Panel
ref	=	Reference condition
T	=	Test section
SV	=	Stern-Volmer calibration
$RANS$	=	Reynolds-averaged Navier-Stokes
W	=	Wedge

Superscripts

$\bar{}$	=	Average
$\hat{}$	=	Prediction

Downloaded by AFRL D'Azzo Wright-Patterson on July 13, 2023 | http://arc.aiaa.org | DOI: 10.2514/6.2023-4134

I. Introduction

Turbulent shock/boundary-layer interactions (SBLIs) represent a key challenge for modern aerospace vehicles. In the mean sense, these interactions can produce sharp gradients in the aerothermal loads, intense three-dimensionality, and separated flow [1, 2]. The unsteadiness associated with separated SBLI [3, 4] is also of concern since the resulting wall pressure fluctuations can exhibit significant low-frequency energy content which may drive a structure at resonance. These extreme aerothermodynamic loads, in combination with compliant structures, result in the potential for highly-nonlinear, dynamic aeroelastic behavior. Thus, accurate characterization of the loading environment is critical to the design and analysis of flight-weight structures.

There is a large body of literature focused on the development and implementation of discrete sensors to characterize the mean and dynamic components of the surface loads for shock-dominated flows [1–3, 5, 6]. These studies have primarily relied on high-frequency, surface mounted pressure transducers capable of providing the unsteady spectral energy content of the incoming turbulent boundary layer as well as the SBLI. This information is crucial for the validation of high-fidelity computational fluid dynamic (CFD) solutions [7] as well as the development of reduced-order fluctuating pressure models [8–11]. However, many of these studies were restricted to two-dimensional and axisymmetric canonical configurations such as compression ramps, impinging shocks, and double cones [7]. For these cases, the three-dimensionality of the flow is generally negligible and a single streamwise array of pressure transducers can be used to map the loading environment. In practical applications (e.g. swept SBLI, shock-shock interactions, structural compliance, and side-wall effects), the interactions are considerably more complex and three-dimensional. As such, it is necessary to measure the full-field surface pressure simultaneously. On their own, conventional surface-mounted transducers are impractical for these applications due to the large number of sensors that are likely required, uncertainty regarding their placement on the test article [12], the excessive costs to instrument a model [13], and the potential for interference with the dynamic response of a compliant structure. Fast-response pressure sensitive paints (fast PSPs) have emerged as a promising supplemental measurement for these configurations [13–15].

Pressure sensitive paints exploit the sensitivity of luminescent molecules to oxygen density through a process known as oxygen quenching [13, 14]. Typically, paint formations include a luminescent molecule, i.e. the luminophore, embedded in an oxygen permeable binder that adheres the luminophore to the model surface [14]. The light intensity emitted by the paint under ultraviolet excitation is a strong function of the oxygen concentration surrounding the luminophore, which in turn is related the local air pressure. Images of the emitted luminescence can then be measured using high-speed cameras and converted to instantaneous surface pressure fields via the Stern-Volmer relation [16]. Many conventional paints rely on a polymer binder. However, the response time of the paint is governed by the rate of diffusion of gas within the polymer. This limits the application of these paints to measuring mean surface pressure. A solution is the application of thinner paint layers, similar to the fast fluoro-isopropyl-butyl (TurboFIB) PSP developed by Innovative Scientific Solutions, Inc. (ISSI). While this approach can improve the frequency response, the paint generally suffers from reduced luminescent intensity, degraded signal-to-noise ratios, and signal attenuation effects. Note that significant efforts have been made to correct for the latter two effects. This includes the development of a diffusion-based model to correct the underprediction of the root mean square (RMS) pressure due to the limited frequency response of the paint [17].

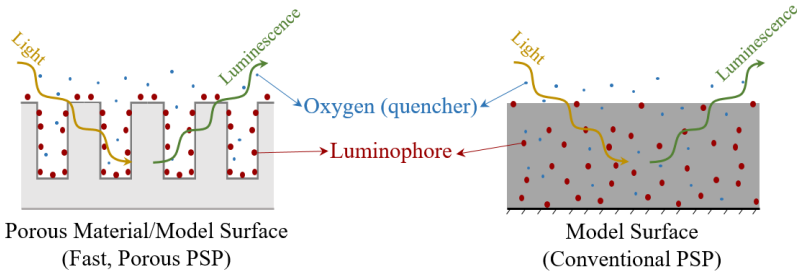

Fig. 1 Comparison of conventional and porous PSP formulations.

An alternate strategy for improving the frequency response of PSP is to increase the diffusivity of the paint binder. This has led to the development of porous materials where the luminophore is directly exposed to the oxygen molecules as opposed to suspended within the binder. This is schematically depicted in Fig. 1. Examples of porous PSP include the polymer-ceramic (PC-PSP) developed by ISSI, which can detect fluctuations up to 20 kHz [18–20], and anodized aluminum (AA-PSP), which has a response time on the order of 10 μs [21, 22]. Experimental configurations that have used ISSI's PC-PSP include transverse jet interactions [18], rectangular cavity flows [20], fin-generated swept SBLI [23], impinging stationary and oscillating SBLI [24–26], and two-dimensional compression ramps [27]. Note that several of the SBLI studies considered the effects of structural compliance. In addition, PSP was routinely used simultaneously with other full-field, non-contact measurements including three-dimensional digital image correlation (DIC), particle image velocimetry (PIV), and high-speed Schlieren. The results have demonstrated that the PC-PSP provides a full-field view of complex, three-dimensional interactions, which is not easily recreated when relying solely on discrete pressure transducers. However, temperature sensitivity remains a dominant source of error for the unsteady PC-PSP measurements. In contrast, Sakaue et al. [22] has developed an AA-PSP with a significantly reduced temperature dependency relative to other paints while retaining a high pressure sensitivity. This formulation has been applied to a variety of geometries in high-speed flow including a half-angle cone/flare model [28, 29], cylindrical duct with a conical intake [30], and compression corner [31].

During a recent entry in the Air Force Research Laboratory (AFRL) Research Cell 19 (RC-19) facility, the porous, fast-response PC-PSP developed by ISSI was used to obtain measurements of the full-field surface pressure for a range of oblique shock impingement conditions over a flat, rigid test article. Traditional pressure transducers were also included in order to calibrate and evaluate the response of the PSP at discrete locations on the surface. The objective of this paper is to use the full-field, unsteady pressure data to characterize the unique loading environment in RC-19 for a range of SBLI conditions. This includes understanding the impact of shock-induced separation, shock sweep, and facility-dependent effects (e.g. sidewall effects and flow asymmetries) on the loads. Note that the measurements obtained from these experiments are not meant to serve as canonical data sets due to the potential for facility-dependent effects. Instead, the data and insights obtained will be key to developing robust and expedient models of the aerodynamic loads in RC-19 which will enable long-duration aeroelastic predictions for shock-dominated flows [32, 33].

The remainder of the paper is organized as follows. The RC-19 experiments are briefly reviewed in Section II. This

Downloaded by AFRL D'Azzo Wright-Patterson on July 13, 2023 | http://arc.aiaa.org | DOI: 10.2514/6.2023-4134

includes an overview of the fast PSP technique. The RANS model is detailed in Section III. The time-averaged pressure loads, including a comparison between simulations and experiments, are presented in Section IV.A. Dynamic pressure measurements are discussed in Section IV.B. Concluding remarks are provided in Section V.

II. Experimental Overview

A brief overview of the RC-19 facility, operating conditions, and instrumentation are provided below. This includes a discussion on the setup and acquisition of fast PSP measurements. For additional information on the setup and characterization of flow in the tunnel, the reader is referred to Spottswood et al. [34] and Brouwer et al. [35].

A. Facility and Geometry

The RC-19 is a continuous Mach 1.5 – 3 supersonic wind tunnel that was previously modified to accommodate both rigid and flexible panels flush with the top wall. The present study used the rigid test specimen which was machined from AISI 4140 alloy steel with the dimensions listed in Table 1. The sides of the tunnel contained large quartz windows to allow for flow-field visualization. The bottom wall also contained a quartz window for full-field PSP illumination and measurements. A shock generating wedge was installed on the wall opposite of the panel as shown in Fig. 2. The wedge location was fixed during testing such that the inviscid shock impingement location occurred just upstream of the midchord. The tunnel operating conditions are provided in Table 2. Note that while the wind tunnel configuration was designed to produce a nominal test section Mach number of 2.0, static pressure measurements upstream and over the test article support the lower value in Table 2.

Table 1 RC-19 test section and rigid specimen geometry.

Parameter	Value
Test section length, L_T (mm)	918
Test section width, W_T (mm)	152
Test section height, H_T (mm)	131
Rigid panel length, L_p (mm)	254
Rigid panel width, W_p (mm)	127
Rigid panel thickness, h_p (mm)	12.7

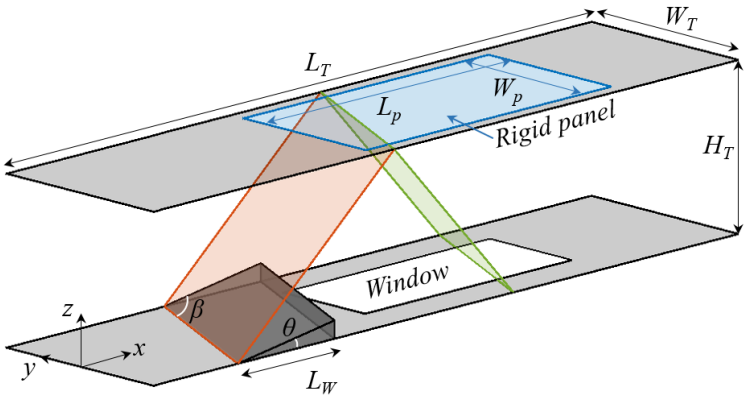

Fig. 2 Schematic of the RC-19 test section with an inviscid oblique shock impingement. The dark gray planes define the wedge, the orange plane is the impinging shock, and the green plane is the reflected shock. The tunnel sidewalls are not shown.

A primary objective of this test campaign was to explore the impact of SBLI on the aerodynamic loads in the absence of structural compliance. Three wedges were constructed to yield nominally two-dimensional SBLI with attached and

Downloaded by AFRL D'Azzo Wright-Patterson on July 13, 2023 | http://arc.aiaa.org | DOI: 10.2514/6.2023-4134

Table 2 Operating conditions.

Parameter	Value
Mach Number, M	1.92
Total pressure, p_0 (kPa)	345
Total temperature, T_0 (K)	290
Reynolds number, Re (m^{-1})	45.6×10^6

separated flow. An additional wedge was also designed to study the effect of swept shock impingements for attached flow. The as-manufactured dimensions for each wedge are listed in Table 3 along with the estimated shock impingement location, x_{Imp}/L_p, and streamwise distance from the wedge leading edge to the panel leading edge, Δx_{wedge}. The latter two values were extracted from available PSP and Schlieren data along the midspan of the tunnel. The impingement location was measured from the leading edge of the thin panel. Note that all of the wedges were approximately 150 *mm* wide. A schematic of the inviscid shock impingement is also provided in Fig. 2.

Table 3 As manufactured shock generating wedge geometries.

Wedge Name	θ (deg)	β (deg)	L_W (mm)	x_{Imp}/L_p	Δx_{Wedge}
4 *deg* wedge	3.9	-	110.8	0.41	0.086
Swept 4 *deg* wedge	4.0	20.3	109.5	0.42	0.095
8 *deg* wedge	8.1	-	70.8	0.43	0.053
12 *deg* wedge	11.6	-	59.7	0.40	0.046

B. Instrumentation

1. Discrete Wall Pressure Measurements

Traditional discrete measurements of surface pressure were included in the experiments. The sensor layout is provided in Fig. 3 (b). Mean surface pressure was recorded at twenty-eight evenly spaced locations on the rigid panel using an electronically scanned pressure (ESP) module. The panel was also instrumented with twenty Kulite XTEL-190 pressure transducers. A majority of the Kulites were placed over the upstream half of the panel along the midspan in order to capture the streamwise shock-induced pressure gradients. Six Kulites were also installed off-center in order to capture three-dimensional effects due to the sidewalls or swept shock impingements. As illustrated in Fig. 3 (b), five of these Kulites stopped working during testing.

All discrete pressure signals were recorded over a period of approximately 10 s at sampling rates of 40 kHz and 1 Hz for the Kulites and ESP, respectively. Note that the discrete sensors and PSP measurements were recorded simultaneously. The ESP data was averaged over the entire time history to obtain the mean pressure distributions. A low-pass filter was applied to the Kulite data to filter frequencies larger than 4 kHz, i.e. the sampling rate of the PSP. The optimal filtering scheme of Naguib et al. [36] was implemented in order to remove low-frequency tunnel noise from the fluctuating wall pressures.

2. Fast, Porous Pressure Sensitive Paint

The commercially available, porous, fast-response paint used in this study is a three component, single-luminophore paint from ISSI and is formulated for unsteady pressure measurements with high pressure sensitivity. The paint has a quoted pressure range of $p = [0, 200]$ kPa, a temperature range of $T = [273, 353]$ K, and a response time of < 100 μs. The paint also has a temperature sensitivity of 3.6% per K, which means that surface temperature variations must be accounted for as part of the pressure calibration process. As will be shown later, this is particularly important for SBLI conditions where shock-induced gradients in the surface temperature are present.

The fast-response PSP is composed of a polymer/ceramic formulation, which provides the porous structure, and the luminescent molecule Platinum Tetra Pentafluorphenyl Porphine (PtTFPP). The paint includes three parts which were

Downloaded by AFRL D'Azzo Wright-Patterson on July 13, 2023 | http://arc.aiaa.org | DOI: 10.2514/6.2023-4134

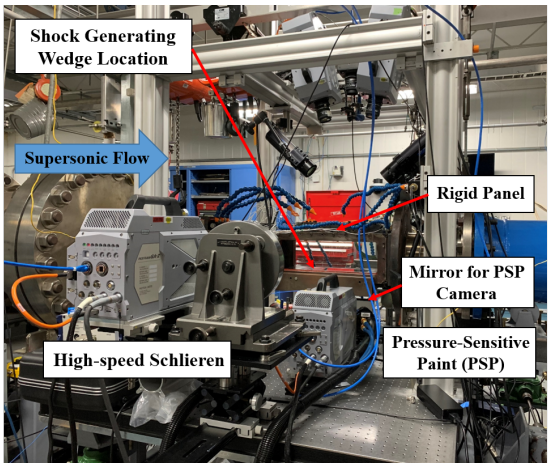

(a) Camera setup.

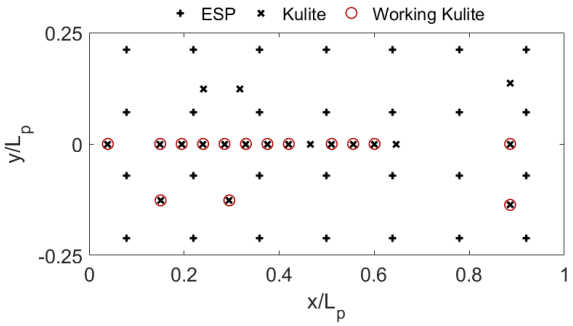

(b) Sensor locations on the rigid panel.

Fig. 3 Rigid panel instrumentation in RC-19.

applied using a spray gun following the procedure provided by ISSI. Illumination for the PSP was provided by two LM2X-400 LED heads entering through the bottom quartz window, as shown in Fig. 3 (a). The lights were triggered on 5 seconds prior to image acquisition and turned off after all images were taken. When excited with 400 *nm* violet light, the luminescence of the paint at 610 *nm* was recorded on a high-speed SA-Z camera through the bottom window, as illustrated in Fig. 3 (a). As mentioned above, the luminescence is a function of the local surface pressure where each pixel in the resulting image acts as a dynamic pressure sensor. Intensity images were recorded at a rate of 4000 fps for approximately 15 s with a resolution of 1024×600 pixels. The resulting scale was 0.3 $mm/pixel$.

A ratio of the intensity images at a known wind-off pressure to the unknown wind-on conditions were computed in order to account for non-uniformities in lighting and paint application. Contaminated regions corresponding to the Kulite and static pressure sensors were removed during post-processing of the PSP data. Calibration was performed *in-situ* during evacuation of the test section for discrete pressures in the range of $[21, 97]$ kPa and the coefficients were computed through a second-order fit of the Stern-Volmer equation [16]:

$$\frac{I_{ref}}{I} = A(T) + B(T)\frac{p_{SV}}{p_{ref}} + C(T)\left(\frac{p_{SV}}{p_{ref}}\right)^2 \tag{1}$$

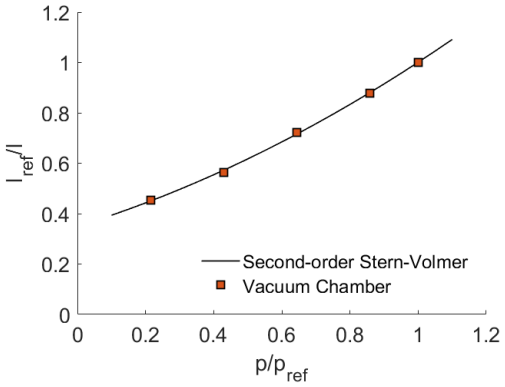

Fig. 4 Fast, porous PSP calibration with least-squares curve fit of Eq. 1.

An example of the resulting fit is provided in Fig. 4 where atmosphere was taken as the reference condition. A similar calibration was computed using images obtained after each of the runs with a different wedge in order to account

Downloaded by AFRL D'Azzo Wright-Patterson on July 13, 2023 | http://arc.aiaa.org | DOI: 10.2514/6.2023-4134

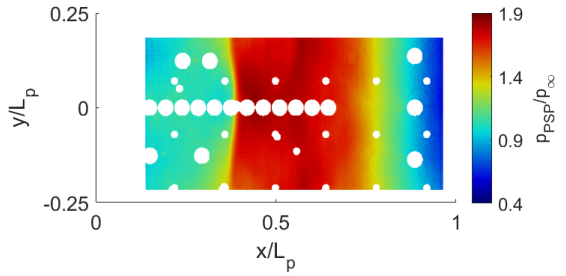

(a) Pressure sensitive paint (PSP) after application of Eq. 1.

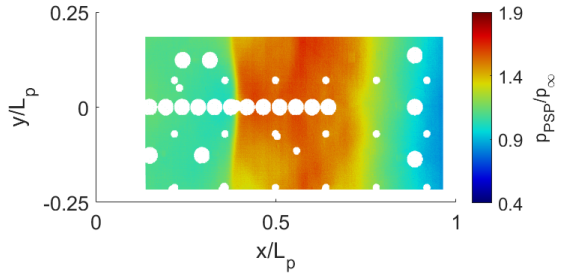

(b) Pressure sensitive paint (PSP) after application of the nonlinear regression model, Eq. 2.

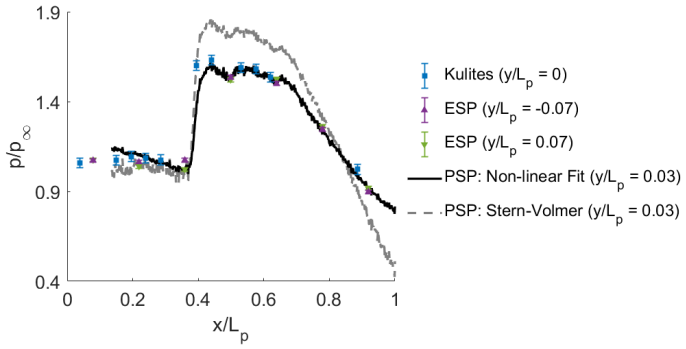

(c) Pressure measurements near the midspan.

Fig. 5 Comparison of mean pressure measurements before and after the nonlinear calibration of the unfiltered PSP. $\theta = 4$ deg, $p_\infty = 49.9$ kPa, $Re_{L_p} = 11.6 \times 10^6$.

for changes in the PSP luminophore response over successive runs. Note that this calibration neglects the variation of the coefficients with temperature since the wind-off images were acquired at a constant value. However, the temperature sensitivity of the paint cannot be ignored for SBLI conditions. Consider the mean pressure measurements for the 4 *deg* wedge in Fig. 5. The PSP calibrated using the second-order Stern-Volmer fit, Fig. 5 (a), accurately captures the pressure upstream, but exhibits large errors in the vicinity of the SBLI due to surface temperature gradients. Although not shown, the errors grow in magnitude with increasing shock strength. In the absence of full-field surface temperature measurements for the rigid article, an array of pressure transducers, Fig. 3 (b), were used to correct the output of the Stern-Volmer equation. A nonlinear regression model, f_{NL}, was constructed:

$$\frac{p}{p_{SV}} = f_{NL}(x, y, p_{SV}) \tag{2}$$

where p is the final temperature-calibrated pressure and p_{SV} is the output of Eq. 1. This model form was selected in order to ensure that the nonlinear surface, f_{NL}, serves as a first-order multiplier to p_{SV}. A support vector machine regression model with a third-order polynomial kernel function was used to approximate f_{NL}. MATLAB's built-in function *fitrsvm* was used to construct this model. The resulting temperature-corrected PSP for the 4 *deg* wedge is provided in Fig. 5 (b) and yields an improvement in the surface pressure measurement relative to the discrete sensors. Note that the above calibration approach is characteristically similar to the methodology outlined in Mears et al. [23].

An in-house MATLAB code was developed to post-process the raw PSP images and convert them to pressure fields. First, the average wind-off intensity image was computed for the reference condition. Next, the wind-on images were manually shifted in order to ensure alignment of the pressure sensors between the wind-on and wind-off images. This operation removes noise that would otherwise be introduced due to movement of the tunnel relative to the camera during testing. Ratios of the reference to wind-on images were computed for each run condition and Eq. 1 was applied to each frame on a pixel-wise basis to obtain the instantaneous pressure fields. The Kulite and static pressure taps were also removed from each image during this step. Next, the regression model in Eq. 2 was fit using the mean pressure from the discrete sensors and $\overline{p_{SV}}$. Note that when fitting the model, $\overline{p_{SV}}$ was not available at the exact sensor location. Therefore, an average of the pixels closest to each sensor location was used as a substitute. The nonlinear regression

Downloaded by AFRL D'Azzo Wright-Patterson on July 13, 2023 | http://arc.aiaa.org | DOI: 10.2514/6.2023-4134

model was applied to all images and the resulting temperature-calibrated pressure fields were spatially filtered using a 13×13 pixel averaging filter. This filter size was selected based on the Kulite diameter [34]. Similar to the Kulites, an optimal filter[36] was applied to remove the tunnel noise from the paint signals.

III. Computational Modeling

The NASA Langley CFL3D code [37, 38] was used to compute the required flow solutions. The code uses an implicit finite volume algorithm based on upwind-biased spatial differencing to solve the RANS equations. Since CFL3D is a RANS solver, closure of the equations is achieved through turbulence modeling. Thus, only a mean prediction of an otherwise dynamic flowfield is obtained and unsteadiness induced by SBLI is not captured [7].

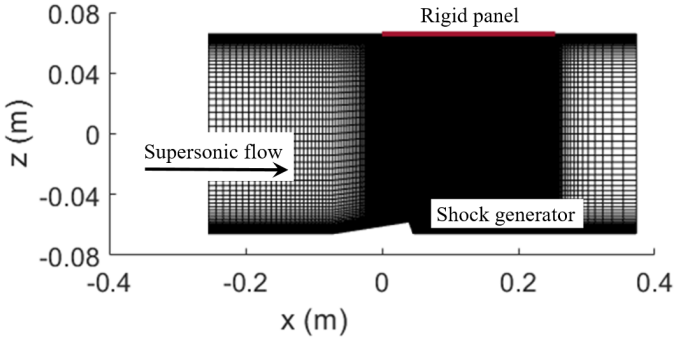

Fig. 6 Reynolds-averaged Navier-Stokes (RANS) mesh.

The computational domain for the RC-19 experiments in Fig. 6 consisted of 501, 193, and 169 points in the x, y, and z-directions, respectfully. Grid points were exponentially distributed away from the tunnel walls in the y and z-directions. The resulting mesh had an average nondimensional wall spacing of 0.25. In addition, 401 and 73 points were evenly distributed over the surface in the x and y-directions, respectively. Grid convergence for this setup was addressed in previous publications [32, 35, 39]. The width and height of the mesh matched those of the tunnel listed in Table 1. The entire tunnel length, i.e. nozzle and test section, was not modeled in order to reduce computational costs. Instead, the upstream boundary of the mesh was located 0.25 m from the rigid panel leading edge. An inflow turbulent boundary layer was specified using the Sun and Childs [40] profile for the outer layer and the Musker [41] profile for the inner viscous sublayer. Note that generation of the velocity profile required the specification of the turbulent boundary layer thickness. This quantity was selected such that the boundary layer thickness at the leading edge of the rigid test specimen matches that reported in Spottswood et al. [34], i.e. $\delta_{TBL} = 8.6\ mm$. The boundary layer temperature profile was specified using the model presented in Whitfield and High [42]. Pressure was assumed to be constant through the boundary layer. No-slip, adiabatic wall boundary conditions were used for all of the tunnel sidewalls. An extrapolation condition was assumed at the downstream boundary of the mesh. The mesh was deformed on the bottom boundary in accordance with the shock-generating wedge geometries listed in Table 3. The as-manufactured wedges had a right triangle profile when viewed from the side. In order to simplify the meshing procedure the trailing edge of the wedges were assumed to have a steep slope, as illustrated in Fig. 6. Although not shown, several different trailing edge angles were considered. For sufficiently steep angles, the trailing edge geometry did not appreciably impact the loading environment over the panel.

The specification of an appropriate turbulence model for a given application remains an area of active research, particularly for SBLI [43–45]. Various turbulence models have been examined for closure of the RANS equations, and in general have been shown to reasonably predict surface pressure, except in the presence of significant flow separation. Two different turbulence models were considered for comparisons with the measured surface pressure: Wilcox (2006) k-ω ($WKW06$) [46] and Menter k-ω shear stress transport (SST) [47]. As demonstrated later, the SST and $WKW06$ models produced nearly identical results for conditions with attached flow and only differed in the presence of significant separation. As such, only the $WKW06$ model results are presented for the unswept and swept 4 deg wedges.

Downloaded by AFRL D'Azzo Wright-Patterson on July 13, 2023 | http://arc.aiaa.org | DOI: 10.2514/6.2023-4134

IV. Results and Discussion

Full-field, time-averaged and unsteady pressure field measurements are presented for each SBLI condition. The mean surface pressures are compared against available discrete Kulite and static pressure tap data. Reynolds-averaged Navier-Stokes (RANS) solutions are also benchmarked using the PSP data. This comparison gives confidence in the loading environment predicted by the RANS model which is used in combination with enriched piston theory to construct reduced-order models of the aerodynamic loads [32, 39]. Note that the measured pressure fields from PSP could also be used to construct such models [11].

Unsteady pressure results are presented in terms of the RMS and power spectral densities (PSDs). Since the computational modeling in this study is restricted to RANS solutions, only the Kulite data are available for comparison with the PSP. Note that Funderbunk and Narayanaswamy [17] developed models to correct unsteady PSP for degraded signal-to-noise ratios and signal attenuation effects. These effects aren't anticipated to be an issue for the current application of PSP given that the paint's reported response time is < 100 μs and the sampling frequency is 4 kHz. Similar to the time-averaged pressure fields, the full-field unsteady data is critical to the development of data-driven, semi-empirical models of the fluctuating component of the loads [11] as well as validation of higher-fidelity CFD solutions (i.e. large-eddy and direct numerical simulations).

Downloaded by AFRL D'Azzo Wright-Patterson on July 13, 2023 | http://arc.aiaa.org | DOI: 10.2514/6.2023-4134

A. Time-Averaged Surface Pressure

The time-averaged, surface pressure is presented in Figs. 7 - 12. The pressure sensor locations have been removed from all of the PSP images. In addition to full-field measurements and predictions, surface pressure near the midspan is also provided. Although not located near the midspan, results from the static pressure taps (ESP) are also shown to highlight any three-dimensionality in the mean pressure. The PSP curves are extracted along $y/L_p = 0.03$ to avoid the influence of the midspan pressure taps on the PSP. For the full-field pressure, the correlation coefficient, r^2, and normalized root mean square error, $NRMSE$, are used to evaluate the RANS predictions relative to the PSP.

$$r^2 = \frac{\left(\sum_{i=1}^{N}\left(p_i - \overline{p}\right)\left(\hat{p}_i - \overline{\hat{p}}\right)\right)^2}{\sum_{i=1}^{N}\left(p_i - \overline{p}\right)^2 \sum_{i=1}^{N}\left(\hat{p}_i - \overline{\hat{p}}\right)^2} \tag{3}$$

$$NRMSE(\%) = 100 \times \frac{\sqrt{\frac{1}{N}\sum_{i=1}^{N}\left|p_i - \hat{p}_i\right|^2}}{\sqrt{\frac{1}{N}\sum_{i=1}^{N}\left|p_i\right|^2}} \tag{4}$$

In Eqs. 3 and 4, p is the measured pressure, $\hat{p}$ is the predicted pressure evaluated at the measurement locations, the bar symbol corresponds to an average value, and N is the total number of points. The correlation coefficient varies between 0 and 1, where a value of 1 corresponds to perfect correlation. The correlation coefficient is used to compare the shapes of the response, whereas the $NRMSE$ aggregates all errors into a single metric. Error metrics are listed in Table 4.

Table 4 Error metrics for predicted mean surface pressure.

	4 *deg* wedge	Swept 4 *deg* wedge	8 *deg* wedge		12 *deg* wedge	
			SST	*WKW*06	*SST*	*WKW*06
r^2	0.960	0.965	0.974	0.987	0.964	0.981
$NRMSE$ (%)	5.05	5.73	4.67	3.81	6.21	5.57

First, consider the mean surface pressures for the 4 *deg* wedge in Fig. 7. While the wedge is nominally two-dimensional, the resulting SBLI on the panel surface exhibits mild three-dimensionality in the incident shock footprint. This result is due to the interaction of the incident shock with the corner flow [48]. The shock generating wedge spans most of the tunnel width, producing a sidewall shock interaction that is characteristically similar to a swept SBLI generated by a vertical fin. While the flow remains attached along the tunnel walls, the shock causes the boundary layer in the top corners to thicken. This produces a series of compression waves which spread the shock-induced pressure rise over a larger streamwise distance near the corner resulting in the upstream facing, concave shock footprint observed in the PSP data. The *WKW*06-based RANS solution exhibits an identical curvature of the incident shock footprint, particularly near the edges of the rigid panel in Fig. 7 (b). Along the panel midspan, the simulated pressure field exhibits

a clear peak immediately downstream of the impingement location. While the measured pressure from both the Kulites and PSP exhibit a similar peak, it is not as pronounced. Note that the peak pressure in the PSP is partially obscured by the Kulites. The interaction of the impinging shock with the corner flow is likely also responsible for the pressure peak. Downstream of the shock impingement, there is a steady decrease in the pressure as the expansion fan from the trailing edge of the wedge impacts the panel. The overall agreement between the simulations and PSP is quite good with an $NRMSE$ and r^2 of 5.05% and 0.960, respectively.

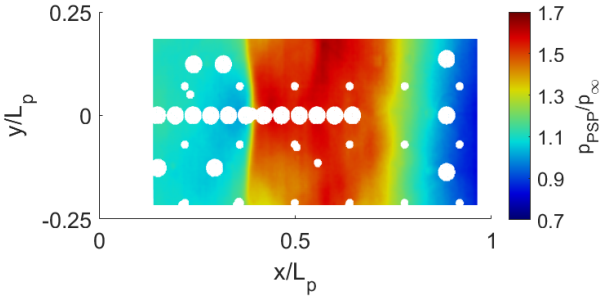

(a) Pressure sensitive paint (PSP).

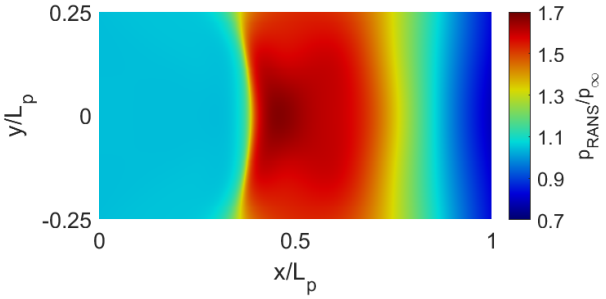

(b) Reynolds-averaged Navier-Stokes (RANS) solution using the $WKW06$ turbulence model [46].

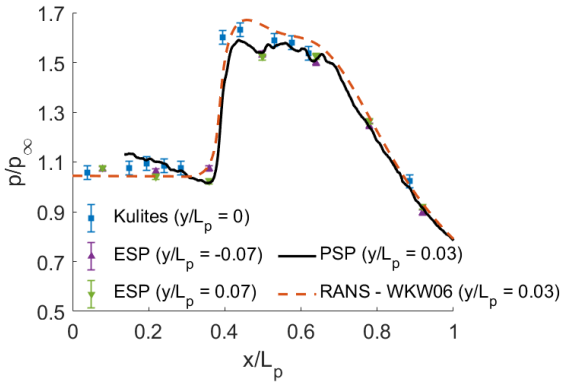

(c) Prediction and measurements near the midspan.

Fig. 7 Comparison of the predicted and measured surface pressure for the 4 *deg* wedge. $p_\infty = 49.9$ kPa**,** $Re_{L_p} = 11.6 \times 10^6$**.**

There is a growing body of work within the SBLI literature focused on swept SBLI configurations. These interactions include swept compression ramps [49–53], sharp fins [23, 54–56], and swept oblique shock impingements [57, 58]. The latter case has been studied extensively in the supersonic wind tunnel at the University of Arizona [58–62]. In order to examine the impact of sweep on the loading environment in RC-19, the 20 *deg* swept 4 *deg* wedge results are provided in Fig. 8. As expected, the tunnel sidewalls have a significant impact on the full-field pressure. Over the lower half of the panel in Fig. 8 (a), the shock footprint exhibits a sweep that is comparable to that of the shock-generating wedge. However, the shock is turned perpendicular to the wall over the upper half of the panel. As will be discussed shortly, this behavior is due to the interaction of the incident shock with the sidewall and is consistent with results published [57]. An apparent reflected shock is also visible downstream over the lower half of the panel, producing a λ-shaped footprint. This feature is visible in both the PSP and $WKW06$-based RANS analysis.

The peak pressure is observed to occur in the PSP data near $(x, y)/L_p = (0.35, 0.125)$. While the simulations predict a similar peak at the same streamwise position, the spanwise location is off by approximately 8.5%. This discrepancy is likely due to differences in the corner flow interaction and/or incoming turbulent boundary layer between simulations and experiments. Another potential (albeit smaller) source of error may be the nonlinear regression model used to correct the PSP for surface temperature effects. Constructing a suitable nonlinear regression model was challenging due to the sparsity of the discrete pressure sensors combined with the nonlinearity of the pressure field. While it is possible that the regression model contributed to the error, a formal uncertainty analysis was not carried out for the PSP data. This dependence on pressure sensors also highlights the need for full-field temperature measurements to properly calibrate the PSP. Obtaining this data is a focus of future work in RC-19. Downstream of the shock impingement there is a gradual decline in the pressure due to the incident expansion fan, similar to the unswept wedge. Overall, the agreement

Downloaded by AFRL D'Azzo Wright-Patterson on July 13, 2023 | http://arc.aiaa.org | DOI: 10.2514/6.2023-4134

in surface pressure between simulation and experiment is reasonable given the error metrics in Table 4.

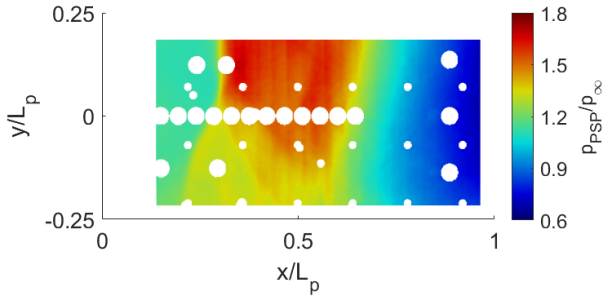

(a) Pressure sensitive paint (PSP).

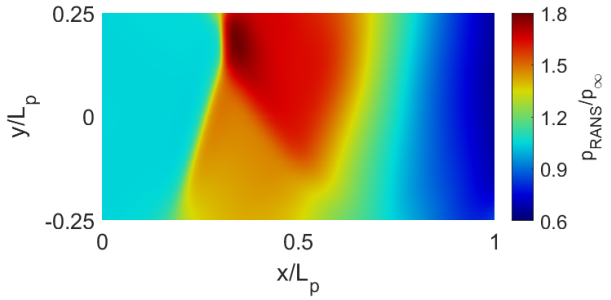

(b) Reynolds-averaged Navier-Stokes (RANS) solution using the $WKW06$ turbulence model [46].

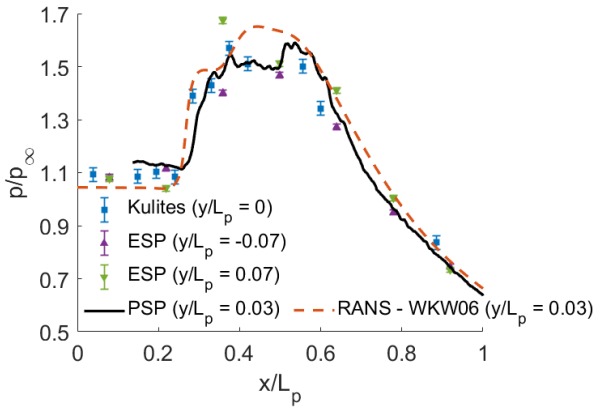

(c) Prediction and measurements near the midspan.

Fig. 8 Comparison of the predicted and measured surface pressure for the 20 *deg* **swept** 4 *deg* **wedge.** p_∞ = 49.9 kPa, $Re_{L_p} = 11.6 \times 10^6$.

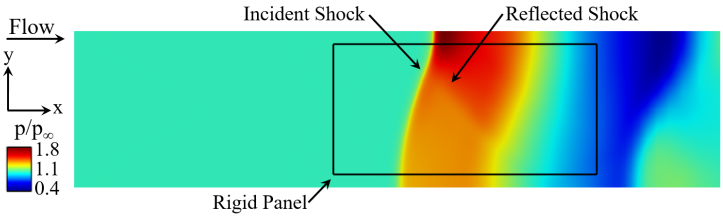

(a) Inviscid pressure contours.

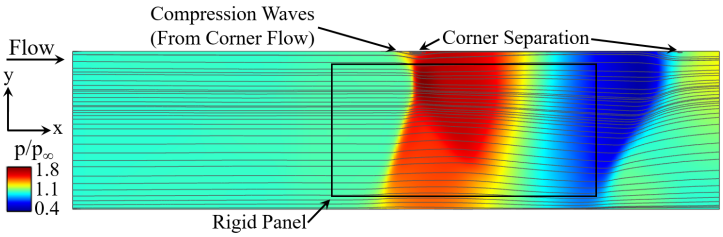

(b) Computational skin friction streamtraces with pressure contours for the $WKW06$ turbulence model [46].

Fig. 9 Computational solutions along the top tunnel wall for the 20 *deg* **swept** 4 *deg* **wedge.** p_∞ = 49.9 kPa, $Re_{L_p} = 11.6 \times 10^6$.

Measurements of the flow-field were not the focus of the present experiments in RC-19. As such, there is limited data on the structure of the shock and expansion waves in the test section. Note that future entries will include a focused

Downloaded by AFRL D'Azzo Wright-Patterson on July 13, 2023 | http://arc.aiaa.org | DOI: 10.2514/6.2023-4134

Schlieren system in order to visualize spanwise slices of the flow-field. This data will be used to further benchmark the RANS models as well as gain an improved understanding of the incident and reflected shock structures. In the absence of this data and given the above comparison, the RANS solutions are used to visualize the predicted flow-field in order to better understand the mechanisms leading to the measured surface pressure in Fig. 8. The inviscid solution for the swept wedge is provided in Fig. 9 (a) for reference. Computational skin friction streamtraces are shown on top of the viscous surface pressure contours in Fig. 9 (b). First, consider the inviscid solution in Fig. 9 (a) which produces a similar shock structure on the top wall of the tunnel. Near the sidewalls, the shock is turned normal to the wall in order to satisfy the zero-crossflow condition at the boundary. Over the lower half of the panel, where the flow is turned away from the lower sidewall, the incident shock sweep mimics that of the wedge. As the upper sidewall is approached, the flow must turn again resulting in the weaker reflected shock highlighted in Fig. 9 (a). Note that the peak pressure occurs at the impingement location along the upper sidewall and is similar in magnitude to the peak value in the viscous solution. The roll-off in pressure observed downstream of the interaction is due to the impinging expansion fan from the trailing edge of the wedge.

Given the similarities between the inviscid and viscous solutions in Fig. 9, the observed shock structure is primarily an inviscid phenomena and the presence of the boundary layer largely serves to compress the spanwise extent of the inviscid, freestream flow in the tunnel. However, there are some noticeable differences. In the viscous solution, the swept incident shock thickens the corner boundary layer which produces a series of weak compression waves. In the lower corner these waves work with the impinging shock to turn the flow away from the sidewall as evidenced by the streamlines downstream of the swept shock. In contrast, the compression waves from the upper corner, $y/L_p = 0.3$, work to turn the flow away from the wall but in the opposite direction of the swept incident shock. This results in the main shock being turned nearly perpendicular to the upper sidewall. The weaker reflected shock from the inviscid solution is also visible over the lower half of the panel. While the incident shock on its own is not strong enough to separate the flow over the panel, the interaction with the sidewall yields a sufficiently large pressure gradient to produce a small region of reversed flow along the upper sidewall. Measurements of undisturbed supersonic corner flows [63] have also demonstrated that the boundary layer profiles are less full than those along the midspan and are therefore prone to separation, even in the presence of relatively weak shocks.

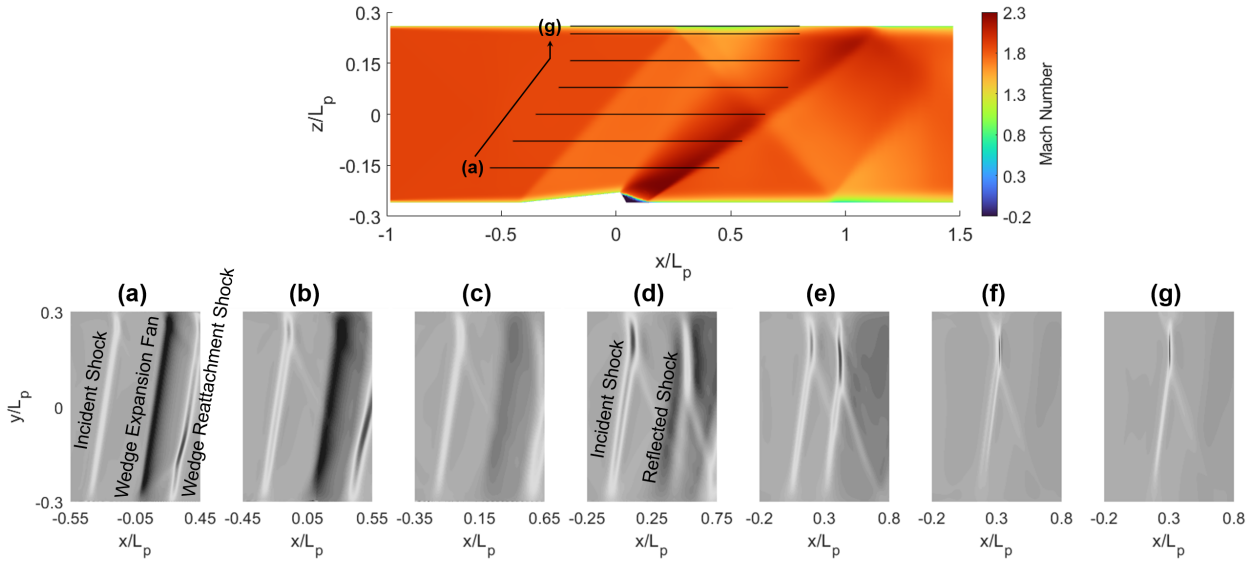

Fig. 10 Distortion of the incident and reflected shocks for the $WKW06$-based RANS analysis. The top image shows Mach number contours along the midspan. The shock structures are illustrated with contours of the streamwise density gradient at selected wall-normal locations. $\theta = 4$ deg, $\beta = 20$ deg, $p_\infty = 49.9$ kPa, $Re_{L_p} = 11.6 \times 10^6$.

The variation of the swept shock structure in the panel normal direction (i.e. z-direction) is also evaluated in Fig. 10. The smaller images show the structure of the shocks and expansion fans using the streamwise density gradients at the wall-normal slices highlighted in the larger image of the Mach contours. At the lowest wall-normal slice, labeled as image (a) in Fig. 10, the impinging shock emanating from the leading edge of the swept wedge is clearly visible. This

Downloaded by AFRL D'Azzo Wright-Patterson on July 13, 2023 | http://arc.aiaa.org | DOI: 10.2514/6.2023-4134

shock remains swept over the entire span of the tunnel, except in the vicinity of the corners where the interaction with the corner boundary layer bends and weakens the shock. There are two other features of note in this first image: the wedge trailing edge expansion fan and reattachment shock. While the expansion fan impacts the surface pressure over the back half of the rigid panel in Fig. 8, the reattachment shock only affects the flow downstream of the panel. Moving in the positive z-direction, the incident shock progressively bends to become perpendicular to the sidewall located at $y/L_p = 0.3$. As mentioned previously, a weaker reflected shock originates from the location where the incident shock turns resulting in the λ-shaped shock structure. This behavior is due to the increasing impact of the interaction between the impinging shock and the tunnel sidewall. The primary reflected shock doesn't appear until image (d) and, as expected, exhibits a similar shape to the incident shock.

Even in the absence of flow separation, the intense three-dimensionality of the loading environment produced by the swept 4 *deg* wedge is of particular interest in the context of compliant structures. For this case, the pressure loading is expected to excite spanwise modes as opposed to the streamwise ones observed in previous post-flutter measurements [32, 35]. Identifying flutter boundaries and exploring the post-flutter behavior for the swept wedge configuration is a focus of ongoing research [33].

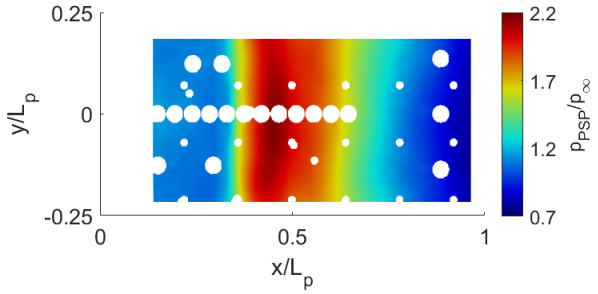

(a) Pressure sensitive paint (PSP).

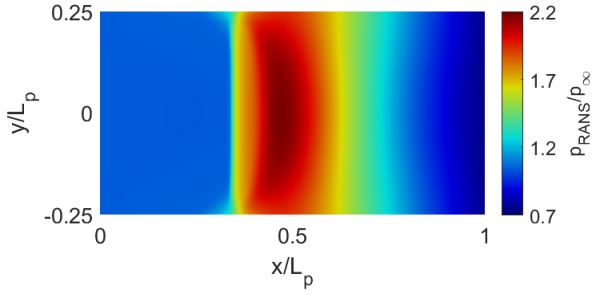

(b) Reynolds-averaged Navier-Stokes (RANS) solution using the $WKW06$ turbulence model [46].

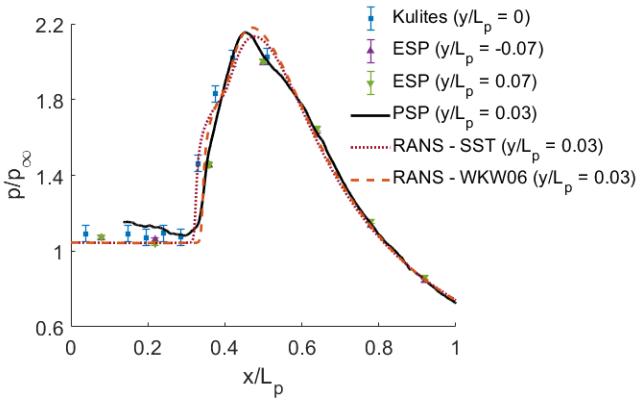

(c) Prediction and measurements near the midspan.

Fig. 11 Comparison of the predicted and measured surface pressure for the 8 *deg* wedge. $p_\infty = 49.9$ kPa**,** $Re_{L_p} = 11.6 \times 10^6$**.**

Mean surface pressure results for the 8 *deg* wedge are provided in Fig. 11. The shock-induced pressure rise occurs just upstream of the panel midchord. The spanwise variation of the reflected shock line is relatively two-dimensional compared to the curvature observed for the unswept 4 *deg* wedge in Fig. 7 (a). This change in shape is due in part to the presence of mild shock-induced separation along the tunnel midspan in combination with the aforementioned corner flow effects. The measured pressure field is increasingly three-dimensional downstream of the peak pressure. The observed behavior is consistent with literature on impinging SBLIs in moderate aspect ratio tunnels [64] and is due to the weak shock waves emanating from the corners which result in an elongated region of an unfavorable pressure gradient centered about the midspan. The $WKW06$-based RANS solution captures the pertinent features of the SBLI pressure loading for this case. In addition, the impact of the corner flows on the reflected shock footprint are visible near the spanwise edges of the panel. While both turbulence models provide a good estimate of the peak pressure and roll-off due to the impinging expansion fan along the midspan, the *SST* model underpredicts the x-location of the initial pressure rise. This is accompanied by an increase in the predicted shock-induced separation length along the midspan

Downloaded by AFRL D'Azzo Wright-Patterson on July 13, 2023 | http://arc.aiaa.org | DOI: 10.2514/6.2023-4134

for the SST model, $0.109L_p$, relative to that predicted by the $WKW06$ model, $0.088L_p$. The variation in the predicted separation lengths is attributed to differences in the turbulent viscosity. The $WKW06$ model predicts an increased turbulent viscosity relative to the SST model, resulting in smaller separation bubbles [65].

The measured and predicted mean pressure loads for the final wedge are provided in Fig. 12. In general, the PSP measurements compare favorably to the Kulite and static pressure ports along the midspan. However, the PSP overestimates the pressure loads upstream of the interaction region relative to the discrete sensors. This difference is likely due to the sparsity of the pressure sensors in the vicinity of the extreme shock-induced pressure gradient which complicates the construction of the nonlinear regression model, Eq. 2, in Sec. II.B.2. An improvement in the agreement would be expected if full-field temperature measurements were available to properly calibrate the PSP. Compared to the 8 *deg* wedge, the region of elevated pressure is significantly larger due to the stronger incident shock and resulting separation bubble generated by the 12 *deg* wedge. The initial pressure rise also exhibits clear three-dimensionality across the span as opposed to the 8 *deg* wedge results. Both wedges exhibit similar characteristics downstream of the interaction. Specifically, an upstream-facing, concave peak pressure line followed by a mildly three-dimensional roll-off in pressure due to the impinging expansion fan from the trailing edge of the wedge.

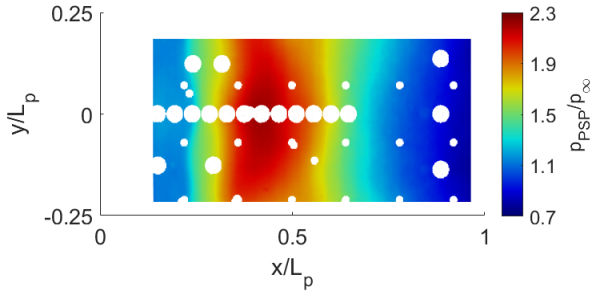

(a) Pressure sensitive paint (PSP).

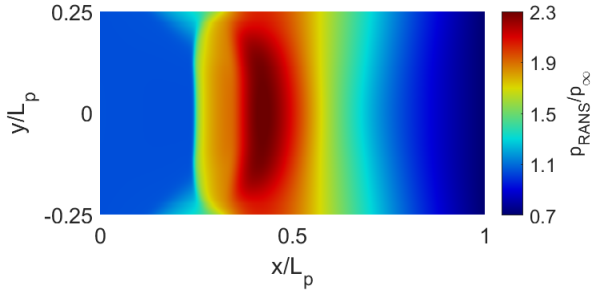

(b) Reynolds-averaged Navier-Stokes (RANS) solution using the $WKW06$ turbulence model [46].

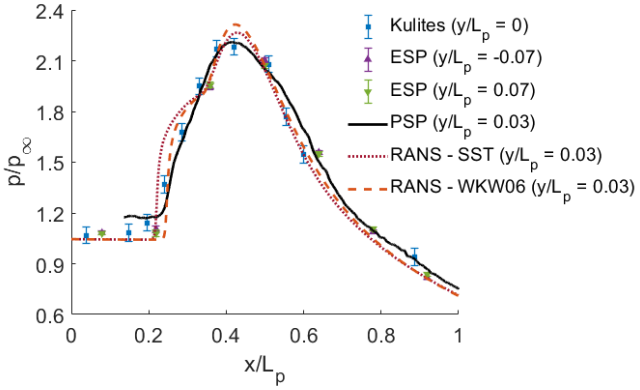

(c) Prediction and measurements near the midspan.

Fig. 12 Comparison of the predicted and measured surface pressure for the 12 *deg* wedge. $p_\infty = 49.9$ kPa**,** $Re_{L_p} = 11.6 \times 10^6$**.**

The $WKW06$ RANS solutions are provided in Fig. 12 (b). Both turbulence model results along the midspan are shown in Fig. 12 (c). The predictions compare favorably to the measured pressure loads with $NRMSE$ and r^2 values for both cases of less than 6.5% and greater than 0.960, respectively. Similar to the previous results, the $WKW06$ model provides superior predictions relative to the SST model due in part to the SST model's overprediction of the midspan separation length, as illustrated in Fig. 12 (c). Here, the prediction separation lengths are $0.174L_p$ and $0.140L_p$ for the SST and $WKW06$ models, respectively. While both turbulence models overshoot the peak pressure, the $WKW06$ prediction is slightly higher. The pressure decline resulting from the impinging expansion fan is reasonably captured by the RANS models. A comparison of the separation shock footprints are provided in Fig. 13 and are defined as the location of the maximum streamwise pressure gradient. Note that the application of a smoothing algorithm was necessary to obtain the experimental shock footprint from the PSP images. Although not necessary, the same algorithm was used for the RANS solutions to obtain consistent results. The $WKW06$ model predicts a very similar footprint with an $NRMSE$ of approximately 6%. The SST model clearly predicts the incorrect shape with an error in excess of 12%.

Downloaded by AFRL D'Azzo Wright-Patterson on July 13, 2023 | http://arc.aiaa.org | DOI: 10.2514/6.2023-4134

As discussed in greater detail below, the elevated error is due to the larger centerline separation bubble predicted by the *SST* model which results in the downstream-facing, concave curvature of the separation shock. In contrast, the *WKW*06 model and the experiments exhibit two peaks near the quarter and three-quarter span. These peaks are due to the weak compression waves emanating from the corner flow.

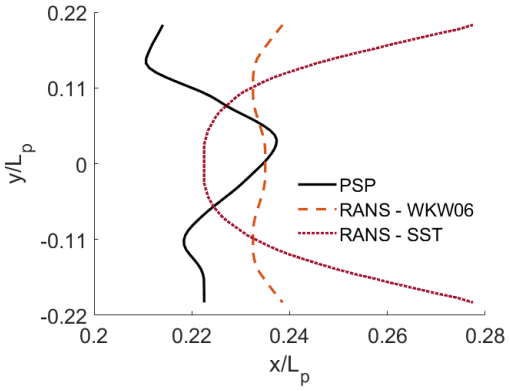

Fig. 13 Comparison of separation shock footprint along the span of the test article for the 12 *deg* **wedge.** $p_\infty = 49.9$ kPa, $Re_{L_p} = 11.6 \times 10^6$.

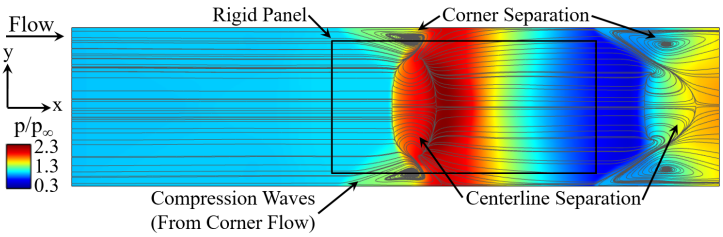

(a) *SST* **turbulence model [47].**

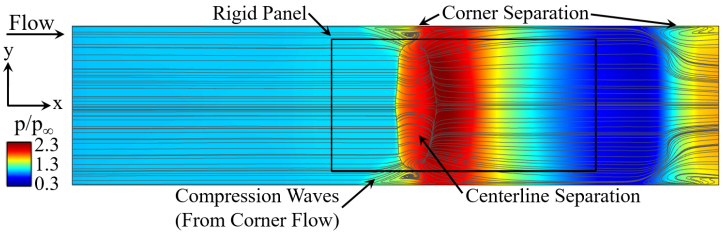

(b) *WKW*06 **turbulence model [46].**

Fig. 14 Computational skin friction streamtraces on the top wall of the RANS solutions for the 12 *deg* **wedge. Pressure contours are also provided.** $p_\infty = 49.9$ kPa, $Re_{L_p} = 11.6 \times 10^6$.

Having benchmarked the RANS simulations, the predicted solutions are used to explore the flow field associated with the pressure distributions in Fig. 12. The computational skin friction streamtraces along the top wall are provided in Fig. 14. Surface pressure contours are also provided for both RANS models. As the incoming flow approaches the impinging SBLI, the corner experiences a rapid thickening and separation upstream of the reflected shock footprint. The corner separation bubbles are clearly visible along the top wall boundaries and upstream of the main centerline separation in both images of Fig. 14. It is important to note the significant variation in separation size between the two turbulence models which is driven by the turbulent viscosity predictions. Specifically, the *WKW*06 model predicts elevated values which result in fuller incoming boundary layer profiles that are less inclined to separation. Since the incoming flow for the *SST* model has a greater tendency to separate, the incident shock and swept SBLI along the tunnel

Downloaded by AFRL D'Azzo Wright-Patterson on July 13, 2023 | http://arc.aiaa.org | DOI: 10.2514/6.2023-4134

sidewall produce larger regions of reversed corner flow which extend to approximately a quarter of the tunnel width. In contrast, the *WKW*06 predicts a corner separation bubble that barely reaches the panel edge, as shown in Fig. 14. A byproduct of this behavior is that the *SST* model produces a significantly more three-dimensional flow-field. The difference in incoming boundary layer profiles is also responsible for the larger centerline separation bubble for the *SST* model compared to the *WKW*06 model. The compression waves emanating from the corner separation are evident in Fig. 14 and eventually interact with and alter the separation shock leading to the footprints provided in Fig. 13. The peaks in the shock footprint approximately occur at the intersection of the compression waves and reflected shock. Another effect of the compression waves is that in the vicinity of the corner, they tend to spread the pressure rise from the reflected shock over a larger distance which produces a milder pressure gradient between the corner and centerline separation regions [64]. In fact, the flow remains attached in this region for both turbulence models. Although not explicitly shown, the size of this attached flow region is smaller for the *SST* model due to the larger separation bubbles. Finally, the centerline separation no longer exhibits the spanwise uniformity of a classical two-dimensional separated SBLI. Instead, the interaction of the compression waves with the separation zone results in an elongation along the centerline [48, 64, 66]. This elongation is considerably more pronounced for the *SST* model.

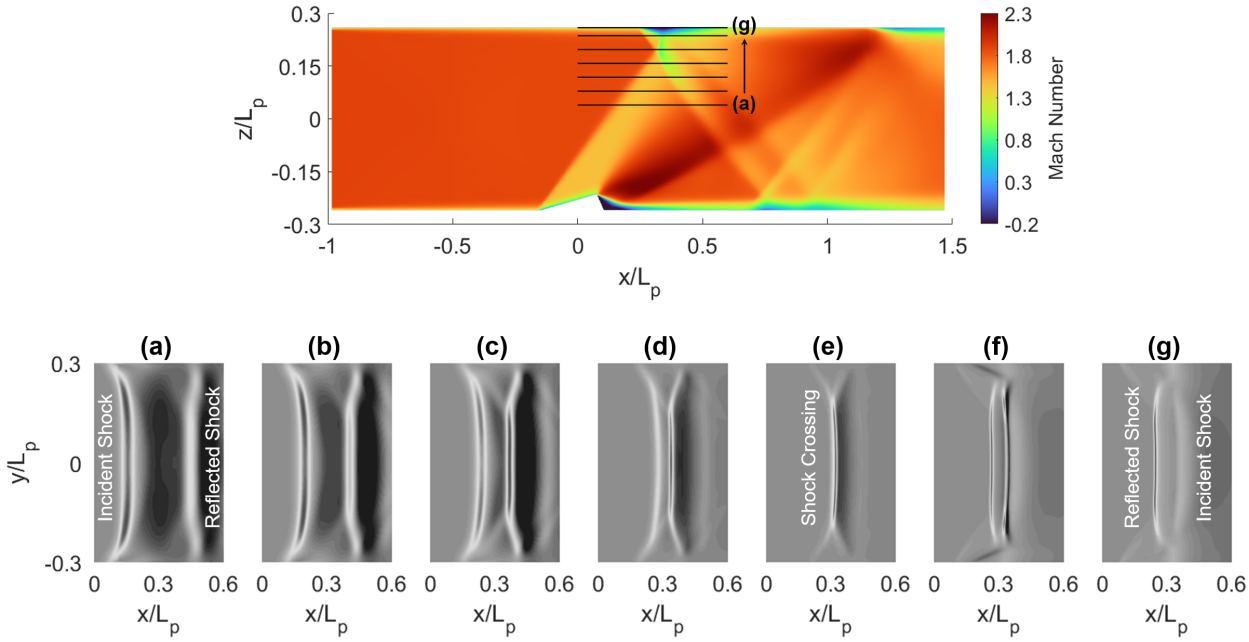

Fig. 15 Distortion of the incident and reflected shocks for the *WKW*06-based RANS analysis. The top image shows Mach number contours along the midspan. The shock structures are illustrated with contours of the streamwise density gradient at selected wall-normal locations. $\theta = 12$ deg, $p_\infty = 49.9$ kPa, $Re_{L_p} = 11.6 \times 10^6$.

The computational skin friction streamtraces illustrate the three-dimensionality of the surface loading for the 12 *deg* wedge. The corner separation bubbles clearly contribute to this behavior. However, the sidewall boundary layer and its interaction with the main impinging shock also play an important role in the three-dimensionality of the flow field. As previously mentioned, the swept SBLI along the sidewalls is similar to the canonical single-fin SBLI geometry which has received significant attention in the literature [23, 54–56]. Note that for the RC-19 configuration, the 12 *deg* wedge does not appear to produce a large enough adverse pressure gradient to separate the flow along the sidewall [54]. However, the sidewall SBLI significantly alters the structure of the incident shock wave, as shown in Fig. 15. Here, the larger image shows the Mach contours along the tunnel midspan, whereas the smaller images provide the streamwise density gradients at a subset of wall-normal locations. Only surface data on the rigid test article was obtained for the present experiments in RC-19. As a result, there is no available measurements of the flow-field to compare with the RANS solutions. Future entries in RC-19 will consider the use of focused Schlieren to obtain spanwise slices of the flow-field for comparison with RANS predictions.

In image (a), the upstream-facing curvature of the incident shock is clearly visible. This shape is a direct result of the interaction with the tunnel sidewall and bottom corner boundary layers. A careful examination of the density

Downloaded by AFRL D'Azzo Wright-Patterson on July 13, 2023 | http://arc.aiaa.org | DOI: 10.2514/6.2023-4134

gradients for the incident shock highlights that the shock strength varies across the span and is strongest near the quarter and three-quarter span. This result is due to the swept SBLI along the sidewall which distorts the impinging shock and increases the pressure gradient across it. An excellent review of a characteristically similar flow-field is provided in [48]. The expansion fan from the trailing edge of the wedge is visible between the incident and reflected shocks in the first three images of Fig. 15. In contrast to the incident shock, the reflected shock in image (a) is clearly weaker near the sidewalls. As discussed earlier, this behavior is due to the compression waves emanating from the corner separation along the top tunnel wall and are clearly visible in the last two images of Fig. 15. The compression waves also intersect with and alter the reflected shock footprint. There is a clear increase in the reflected shock strength near this intersection. Again, the results for the $WKW06$ model are consistent with the measured footprint in Fig. 13.

B. Unsteady Surface Pressure

1. Root Mean Square Pressure Field

The RMS of the unsteady pressure signals, normalized by the freestream dynamic pressure, are shown in Figs. 16 - 19. A comparison of the Kulites and PSP along the midspan is provided in addition to the full-field PSP data. Similar to the mean pressure, the PSP slice is offset from the midspan in order to avoid the influence of the pressure transducers on the paint response. The unswept 4 *deg* wedge produces a relatively small peak in the RMS pressure at the location of the incident shock. Similar to the mean pressure, the peak RMS has a concave curvature across the span due to the interaction of the corner flows with the incident shock. Surprisingly, there is some asymmetry across the span of the RMS peak. A possible explanation is that the incoming flow has a slight angle. However, an in-depth characterization of the tunnel flow without SBLI has not been conducted. Downstream of the peak, the RMS pressure rapidly drops off and returns to the attached turbulent boundary layer levels observed prior to the shock impingement.

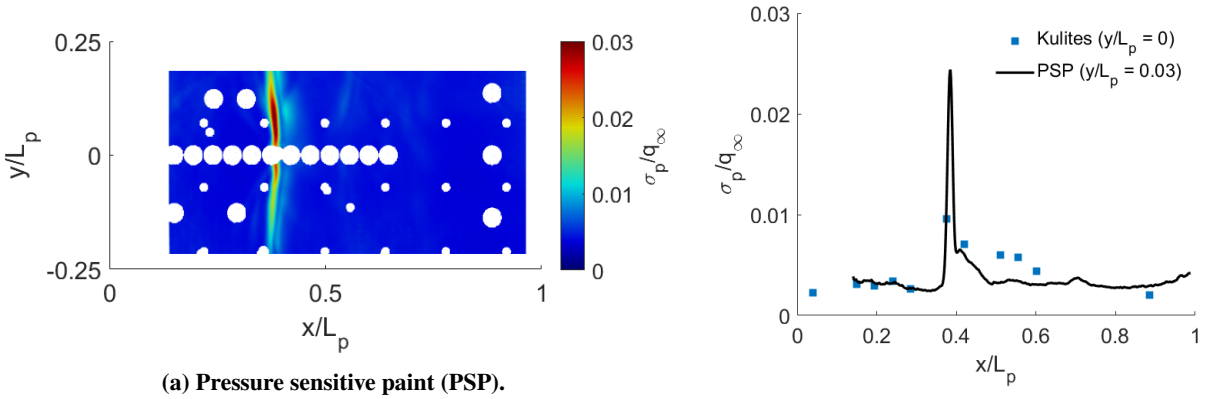

(a) Pressure sensitive paint (PSP).

(b) Comparison between PSP and Kulites.

Fig. 16 Measured RMS pressure for the 4 *deg* **wedge.** $p_\infty = 49.9$ kPa**,** $Re_{L_p} = 11.6 \times 10^6$**.**

The sparsity of the Kulite array along the midspan limits the ability to precisely capture the shock-induced RMS pressure peak. This further highlights the advantage of full-field PSP over discrete sensors. Specifically, only a limited number of pressure sensors were available for use due to cost and tunnel limitations. As such, the sensor locations were carefully selected to ensure that potential regions of interest were adequately represented. In the absence of experimental data, RANS analyses were used to identify these regions resulting in some uncertainty in the sensor locations. In contrast, PSP doesn't require *a priori* knowledge of the loading environment and provides continuous information on how the dynamic pressure changes through the SBLI. Regardless of these issues, there appears to be good agreement in the location of the peak between the two measurements. Downstream of the shock impingement, the Kulites exhibit a more gradual decline in the RMS pressure before returning to the attached turbulent boundary layer levels near the three-quarter chord. The PSP also overestimates the RMS pressure of the furtherest downstream Kulite. While these discrepancies are still under investigation, possible explanations include unsteady signal attenuation and non-trivial residual noise in the PSP dataset.

Downloaded by AFRL D'Azzo Wright-Patterson on July 13, 2023 | http://arc.aiaa.org | DOI: 10.2514/6.2023-4134

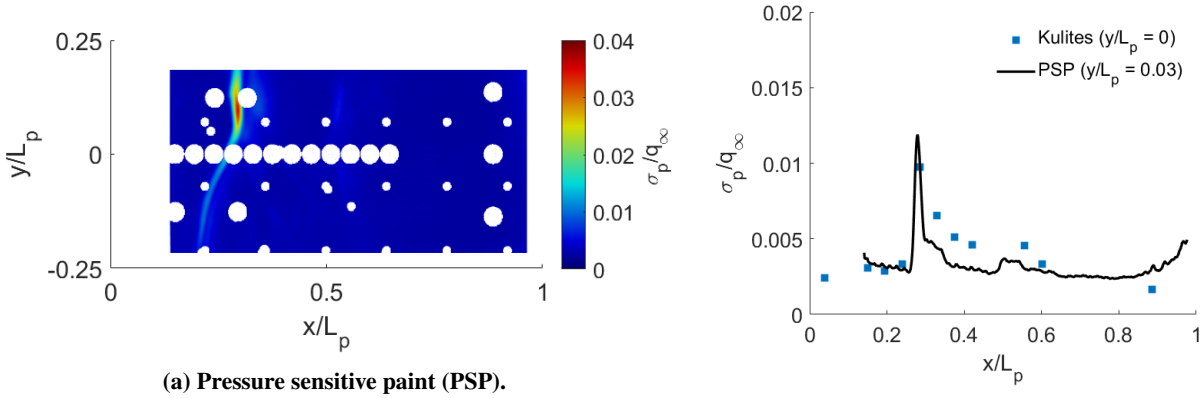

(a) Pressure sensitive paint (PSP).

(b) Comparison between PSP and Kulites.

Fig. 17 Measured RMS pressure for the 20 *deg* **swept** 4 *deg* **wedge.** $p_\infty = 49.9$ kPa**,** $Re_{L_p} = 11.6 \times 10^6$**.**

The three-dimensionality of the unsteady pressure field is more pronounced as the impinging shock is swept relative to the incoming flow. Over the lower half of the panel, $y/L_p < 0$, the peak RMS line is swept by approximately 20 *deg* but turns perpendicular to the sidewall as the upper edge of the panel is approached. This behavior is consistent with the mean pressure field and is due to the interaction between the sidewall swept SBLI, the corner flow, and the incident shock. There is a peak in the RMS pressure ($\sigma_p = 0.04 q_\infty$) which corresponds to the location of the maximum pressure in Fig. 8. This peak is slightly elevated compared to the maximum RMS for the unswept wedge. Note that the peak was not observed in the Kulites due to their sparsity. Possible explanations for the peak RMS include the tunnel inflow asymmetry as well as sidewall effects. Since the peak is coincident with the maximum time-averaged pressure, which appears in both the simulations and experiments, the latter explanation seems to be more plausible as the simulations do not account for tunnel inflow asymmetry. Along the midspan, there is good agreement between the two measurements in the location and value of the initial shock-induced RMS pressure rise. The PSP does overestimate the drop in RMS pressure behind the incident shock. As noted, this discrepancy is a subject of ongoing research. There is a second, albeit smaller, peak which occurs near $x/L_p = 0.5$ and is visible in both the PSP and Kulites. This peak is a byproduct of the weaker reflected shock discussed in Sec. IV.A.

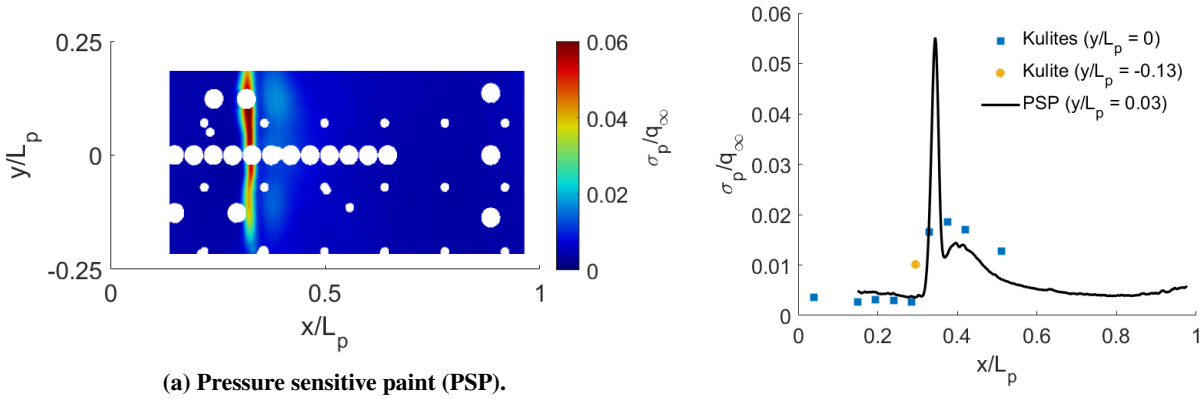

(a) Pressure sensitive paint (PSP).

(b) Comparison between PSP and Kulites.

Fig. 18 Measured RMS pressure for the 8 *deg* **wedge.** $p_\infty = 49.9$ kPa**,** $Re_{L_p} = 11.6 \times 10^6$**.**

The RMS pressure fields for the separated SBLI conditions are shown in Figs. 18 and 19. While the peak RMS is slightly higher for the 12 *deg* wedge, the RMS measurements are characteristically similar for both SBLI conditions. Upstream of the impingement, the RMS value is approximately constant and consistent with an undisturbed turbulent boundary layer. There is a sharp increase in the RMS level near the onset of shock-induced separation. Similar to the mean pressure loading, there is spanwise non-uniformity in the peak RMS. This result is due to the compression waves

Downloaded by AFRL D'Azzo Wright-Patterson on July 13, 2023 | http://arc.aiaa.org | DOI: 10.2514/6.2023-4134

emanating from the corner flow which impinge on the reflected shock resulting in elevated RMS values. The smallest peak RMS pressure from the PSP appears to occur along the midspan. However, the presence of the pressure sensors obscured the PSP data in this region. Similar to the results for the unswept 4 *deg* wedge, there is some asymmetry in the RMS pressure field for both the 8 *deg* and 12 *deg* wedges which appears to follow a similar trend irrespective of the wedge. As mentioned above, this suggests a facility-dependent mechanism in the incoming flow. A second peak due to reattachment of the flow is observed to occur immediately downstream of the separation peak. As expected, this peak is broader with a smaller amplitude. The distance between these two peaks, which is an estimate of the experimental shock-induced separation length, is approximately $0.08L_p$ for the 8 *deg* wedge and $0.12L_p$ for the 12 *deg* wedge. These values are consistent with the RANS solutions reported in Sec. IV.A and support the accuracy of those predictions.

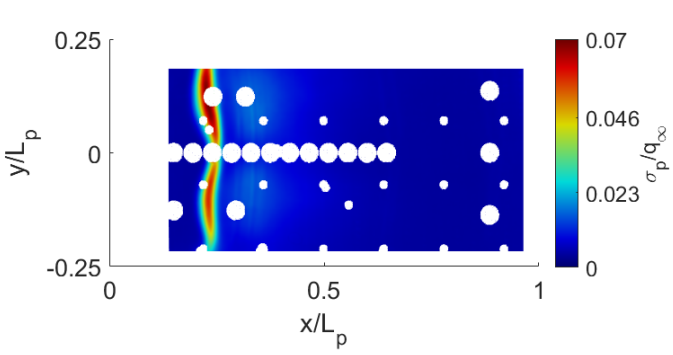

(a) Pressure sensitive paint (PSP).

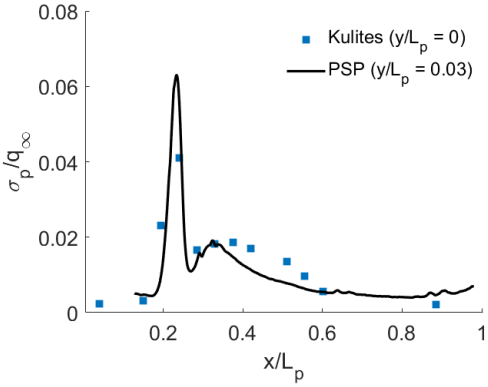

(b) Comparison between PSP and Kulites.

Fig. 19 Measured RMS pressure for the 12 *deg* **wedge.** $p_\infty = 49.9$ kPa, $Re_{L_p} = 11.6 \times 10^6$.

A comparison of the PSP and Kulite RMS pressure along the midspan is provided in part (b) of both figures. Again, there is excellent agreement between the two measurements in terms of the location of the peaks. An off-span Kulite within the intermittent region is provided for the 8 *deg* wedge case in Fig. 18 (b). Note that none of the working Kulites located off of the midspan captured the intermittent region for the 12 *deg* wedge case. Downstream of the shock impingement, the PSP continues to initially underestimate the RMS pressure compared to the Kulites. The PSP then overshoots the Kulite measurement near the panel trailing edge. As noted, these results are still under investigation. Regardless, the above comparisons are encouraging and demonstrate that the PSP can capture the pertinent features for the shock-induced RMS pressure field.

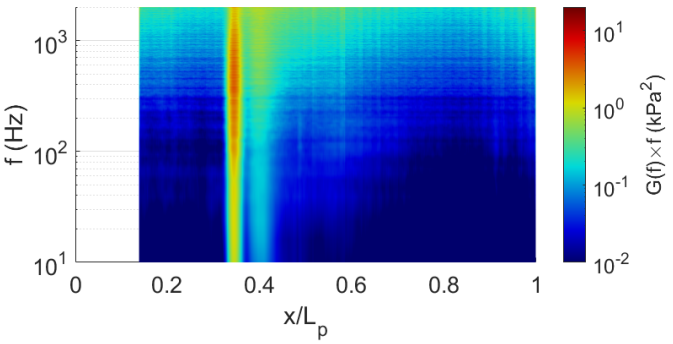

(a) Pressure sensitive paint (PSP). $y/L_p = -0.16$.

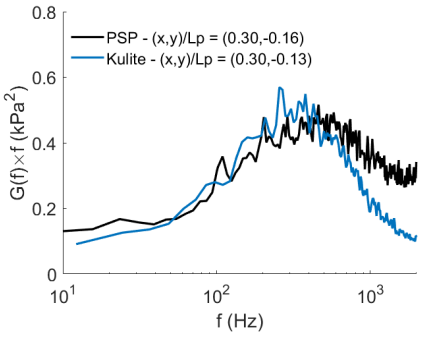

(b) Comparison between PSP and Kulites in the intermittent region.

Fig. 20 Measured pressure PSD for the 8 *deg* **wedge.** $p_\infty = 49.9$ kPa, $Re_{L_p} = 11.6 \times 10^6$.

Downloaded by AFRL D'Azzo Wright-Patterson on July 13, 2023 | http://arc.aiaa.org | DOI: 10.2514/6.2023-4134

2. Unsteady Pressure Spectra

The power spectral densities (PSDs) of the unsteady pressure are presented in Figs. 20 and 21. Only the results for the 8 *deg* and 12 *deg* wedges are presented due to the presence of shock-induced separation and the accompanying low-frequency shock oscillations for these cases. The spatial averaging filter discussed in Sec. II.B.2 was applied to all PSP data. Pressure spectra were computed via Welch's method of windowed Fourier transforms using 512-point segments with 50 % overlap. Each segment was windowed with a Hamming window. The resulting frequency resolution was approximately 8 Hz. Note that the Kulites were down-sampled to the same frequency as the PSP in order to provide one-to-one comparisons between the two measurements. The pressure power, $G(f)$, was pre-multiplied by f to enable direct comparisons in unsteady energy content across all resolvable frequencies. The measured PSP pressure spectra along a streamwise slice are provided for both wedge conditions in Figs. 20 (a) and 21 (a). Power spectral densities in the intermittent SBLI region are compared in part (b) of each figure. Note that the off-span Kulite in Fig. 18 (b) is used for comparison with the 8 *deg* wedge PSP data.

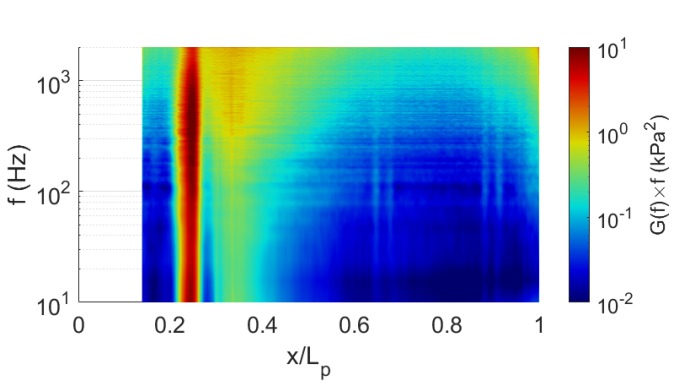

(a) Pressure sensitive paint (PSP). $y/L_p = 0.03$.

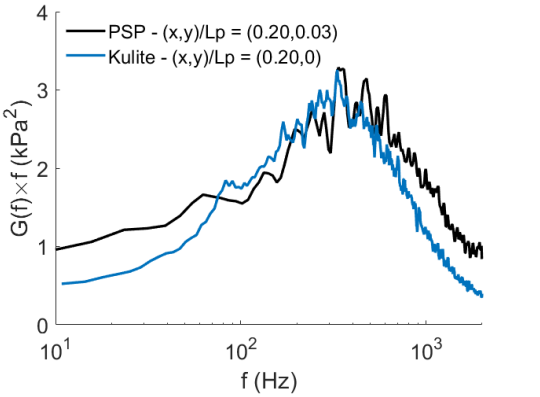

(b) Comparison between PSP and Kulites in the intermittent region.

Fig. 21 Measured pressure PSD for the 12 *deg* **wedge.** $p_\infty = 49.9$ kPa, $Re_{L_p} = 11.6 \times 10^6$.

A comparison of the PSP pressure spectra along the streamwise direction highlights similar SBLI features for both wedge conditions. Upstream of the shock impingement, there is an increase in the pre-multiplied power with frequency, which is characteristic of undisturbed turbulent boundary layer flows. At the onset of the SBLI there is a sharp increase in the power and the peak shifts to lower frequencies indicating the presence of shock oscillations. This is a relatively broadband peak centered about frequencies of approximately 428 Hz and 355 Hz for the 8 *deg* and 12 *deg* wedges, respectively. The frequency for the 8 *deg* wedge is slightly larger due to the smaller separation length. When normalized by the freestream velocity, U_∞, and the predicted separation lengths reported in Sec. IV.A, the non-dimensional Strouhal numbers (St) are 0.021 and 0.025 for the 8 *deg* and 12 *deg* wedges, respectively. Note that these values are within the reported range for low-frequency oscillations associated with separated SBLI. Due to the different incident shock strengths and the resulting separations lengths, the onset of the SBLI for the 12 *deg* wedge occurs just upstream of the location for the 8 *deg* wedge. This is consistent with the time-averaged pressure distributions reported earlier. A second, less prominent peak is observed in both SBLI cases immediately downstream of the separation-induced peak and is associated with reattachment of the flow. As expected, both peaks align with those in the RMS pressure.

The pressure spectra for the PSP and Kulite are compared within the intermittent region in Figs. 20 (b) and 21 (b). The results clearly indicate that both methods capture the broadband, low-frequency unsteadiness associated with the separation shock motion. However, the PSP does overestimate the frequency associated with the peak power. For the 8 *deg* and 12 *deg* wedges, the Kulites display peaks centered about 384 Hz and 316 Hz, respectively. This is an error of approximately 12% for both cases. The PSP also overestimates the power at higher frequencies. While this discrepancy is not fully understood, it is possible that there is a non-trivial residual noise in the PSP data that is influencing the PSDs. Aliasing of the PSP may also be a concern and could potentially explain the shift in shock frequencies when comparing the PSP and Kulites. Addressing these issues will be a focus of future research.

Downloaded by AFRL D'Azzo Wright-Patterson on July 13, 2023 | http://arc.aiaa.org | DOI: 10.2514/6.2023-4134

V. Concluding Remarks

Spatially resolved, time-averaged and unsteady surface pressures in the presence of turbulent shock/boundary layer interactions (SBLIs) were obtained using pressure sensitive paint (PSP). Several shock generating wedges were considered providing SBLI conditions ranging from attached to separated flow. Shock sweep effects were investigated for attached SBLI. Traditional, discrete pressure measurements (i.e Kulites and static pressure sensors) were also used. *In-situ* calibration of the PSP was performed using images obtained at discrete pressures during evacuation of the test section. Since the wall temperature was approximately constant during the acquisition of these images, the resulting calibration did not account for temperature effects. A nonlinear regression model was constructed using the discrete pressure sensors in order to correct the calibrated PSP images for shock-induced surface temperature gradients. Note that the sparsity of the discrete pressure sensors proved to be a challenge in constructing a suitable regression model. This issue likely increased the error in the PSP results. However, a formal calculation of the PSP uncertainty was not conducted. Access to full-field temperature measurements would eliminate the need for the nonlinear regression model. Obtaining this data is a focus of future entries in RC-19. Reynolds-averaged Navier-Stokes (RANS) solutions for each wedge condition were also computed and compared with the measured time-averaged pressure fields. Two different turbulence models were considered.

For attached flow conditions, all of the RANS solutions exhibit good agreement with regard to the mean pressure loading. Normalized root mean square errors (NRMSEs) are less than 6% and correlation coefficients are larger than 0.96 for all of these cases. The swept 4 *deg* wedge predictions have the largest errors relative to the PSP for the attached flow cases. A partial explanation for this discrepancy is the difference in the corner flow and sidewall shock interactions between the simulations and experiments. As mentioned above, the nonlinear regression model used to correct the PSP for temperature effects may have also contributed to the differences. The error metrics for the RANS solutions do not appreciably increase as SBLI strength grows. However, the turbulence model predictions do deviate from each other with the Wilcox $k-\omega$ (2006) turbulence model providing minor improvements in the predicted mean pressure field. While the shock-induced pressure rise is relatively two-dimensional for the 8 *deg* wedge, the 12 *deg* wedge produces a highly three-dimensional flow field. The three-dimensionality of the flow is driven by the swept SBLI along the tunnel sidewalls as well as the interaction of the SBLI with the corner flow along the top tunnel wall. In regard to the unsteady pressure field, the PSP captures the general trends of the root mean square (RMS) pressure relative to the traditional Kulite sensors. Immediately downstream of the shock impingement, the PSP consistently underestimates the RMS pressure as it returns to the undisturbed turbulent boundary layer levels. In the intermittent SBLI region, both unsteady pressure measurement techniques capture the broadband, low-frequency shock oscillations reported in the SBLI literature. However, the PSP overestimates the frequency of the peak power as well as the power at higher frequencies. Note that the error in the frequency is approximately 12 % for both the 8 *deg* and 12 *deg* wedges.

The full-field, non-contact PSP measurements clearly afford valuable insight into the loading environment over the entire test article. However, additional work is needed in order to ensure that the PSP accurately captures the dynamic component of the pressure loads. This may include the implementation of models published in the literature to correct the unsteady PSP for degraded signal-to-noise ratios and signal attenuation effects. Nevertheless, the time-averaged surface pressures obtained from PSP are critical for benchmarking RANS solutions which are in turn used in the construction of reduced-order fluid models. Information on the dynamic component of the pressure is also essential for the development of data-driven, reduced-order fluctuating pressure models that incorporate turbulent boundary layer acoustics as well as low-frequency shock oscillations from separated SBLI. These models will enable robust predictions of the highly nonlinear loading environments for shock-dominated flows.

Downloaded by AFRL D'Azzo Wright-Patterson on July 13, 2023 | http://arc.aiaa.org | DOI: 10.2514/6.2023-4134

Acknowledgments

This research was sponsored by the Air Force Office of Scientific Research (AFOSR) Multi-scale Structural Mechanics and Prognosis and High-Speed Aerodynamics Programs via research grant number 21RQCOR027. The authors gratefully acknowledge the support of AFOSR program manager Sarah Popkin. The authors would also like to thank Innovative Scientific Solutions Inc. (Paul Gross and Justin Hardman) for their wind-tunnel and full-field measurement support as well as Steve Hammack (AFRL/RQHF). This work was supported in part by high-performance computer time and resources from the DoD High Performance Computing Modernization Program.

References

[1] Delery, J., Marvin, J. G., and Reshotko, E., "Shock-Wave Boundary Layer Interactions," No. AGARD-AG-280, 1986.

[2] Dolling, D. S., "Fifty Years of Shock-Wave/Boundary-Layer Interaction Research: What Next? ," AIAA Journal, Vol. 39, No. 8, 2001, pp. 1517–1531.
doi: 10.2514/2.1476.

[3] Coe, C. F., and Chyu, W. J., "Pressure-Fluctuation Inputs and Response of Panels Underlying Attached and Separated Supersonic Turbulent Boundary Layer," AGARD Symposium on Acoustic Fatigue, 1972.

[4] Clemens, N. T., and Narayanaswamy, V., "Low-Frequency Unsteadiness of Shock Wave/Turbulent Boundary Layer Interactions," Annual Review of Fluid Mechanics, Vol. 46, 2014, pp. 469–492.
doi: 10.1146/annurev-fluid-010313-141346.

[5] Adamson, T. C., and Messiter, A. F., "Analysis of Two-Dimensional Interactions Between Shock Waves and Boundary Layers," Annual Review of Fluid Mechanics, Vol. 12, 1980, pp. 103–138.
doi: 10.1146/annurev.fl.12.010180.000535.

[6] Zheltovodov, A. A., "Some Advances in Research of Shock Wave Turbulent Boundary Layer Interactions," AIAA Paper 2006-0496, 2006.
doi: 10.2514/6.2006-496.

[7] Gaitonde, D., "Progress in Shock Wave/Boundary Layer Interactions," Progress in Aerospace Sciences, Vol. 72, 2015, pp. 80–99.
doi: 10.1016/j.paerosci.2014.09.002.

[8] Laganelli, A. L., Martellucci, A., and Shaw, L. L., "Wall Pressure Fluctuations in Attached Boundary-Layer Flow," AIAA Journal, Vol. 21, No. 4, 1983, pp. 495–502.
doi: 10.2514/3.8105.

[9] Laganelli, A. L., and Wolfe, H. F., "Prediction of Fluctuating Pressure in Attached and Separated Turbulent Boundary-Layer Flow," Journal of Aircraft, Vol. 30, No. 6, 1993, pp. 962–970.
doi: 10.2514/3.8105.

[10] Deshmukh, R., Culler, A. J., Miller, B. A., and McNamara, J. J., "Response of Skin Panels to Combined Self- and Boundary Layer-Induced Fluctuating Pressure," Journal of Fluids and Structures, Vol. 58, 2015, pp. 216–235.
doi: 10.1016/j.jfluidstructs.2015.08.008.

[11] Freydin, M., Dowell, E. H., Varigonda, S. V., and Narayanaswamy, V., "Response of a Plate with Piezoelectric Elements to Turbulent Pressure Fluctuation in Supersonic Flow," Journal of Fluids and Structures, Vol. 114, 2022, pp. 1–42.
doi: 10.1016/j.jfluidstructs.2022.103696.

[12] Riley, Z. B., Perez, R. A., Bartram, G. W., Spottswood, S. M., Smarslok, B. P., and Beberniss, T. J., "Aerothermoelastic Experimental Design for the AEDC/VKF Tunnel C: Challenges Associated with Measuring the Response of Flexible Panels in High-temperature, High-speed Wind Tunnels," Journal of Sound and Vibration, Vol. 441, 2019, pp. 96–105.
doi: 10.1016/j.jsv.2018.10.022.

[13] McLachlan, B. G., and Bell, J. H., "Pressure-Sensitive Paint in Aerodynamic Testing," Experimental Thermal and Fluid Science, Vol. 10, No. 4, 1995, pp. 470–485.
doi: 10.1016/0894-1777(94)00123-P.

[14] Gregory, J., Asai, K., Kameda, M., Liu, T., and Sullivan, J., "A Review of Pressure-Sensitive Paint for High-Speed and Unsteady Aerodynamics," Proceedings of the Institution of Mechanical Engineers, Part G: Journal of Aerospace Engineering, Vol. 222, No. 2, 2008, pp. 249–290.
doi: 10.1243/09544100JAERO243.

[15] Gregory, J., Sakaue, H., Liu, T., and Sullivan, J., "Fast Pressure-Sensitive Paint for Flow and Acoustic Diagnostics," Annual Review of Fluid Mechanics, Vol. 46, 2014, pp. 303–330.
doi: 10.1146/annurev-fluid-010313-141304.

[16] Stern, O., and Volmer, M., "Uber die Abklingungszeit der Fluoreszenz," Physikalische Zeitschrift, Vol. 20, No. 8, 1919, pp. 183–188.
doi: 10.1007/978-3-662-46962-0_5.

[17] Funderbunk, M. L., and Narayanaswamy, V., "Spectral Signal Quality of Fast Pressure Sensitive Paint Measurements in Turbulent Shock-Wave/Boundary Layer Interactions," Experiments in Fluids, Vol. 60, No. 154, 2019, pp. 1–20.
doi: 10.1007/s00348-019-2799-x.

Downloaded by AFRL D'Azzo Wright-Patterson on July 13, 2023 | http://arc.aiaa.org | DOI: 10.2514/6.2023-4134

[18] Crafton, J. W., Forlines, A., Palluconi, S., Hsu, K. Y., Carter, C., and Gruber, M., "Investigation of Transverse Jet Injections in a Supersonic Crossflow Using Fast-Responding Pressure-Sensitive Paint," Experiments in Fluids, Vol. 56, No. 27, 2015, pp. 1–15.
doi: 10.1007/s00348-014-1877-3.

[19] Sellers, M. E., Nelson, M. A., and Crafton, J. W., "Dynamic Pressure-Sensitive Paint Demonstration in AEDC Propulsion Wind Tunnel 16T*," AIAA Paper 2016-1146, 2016.
doi: 10.2514/6.2016-1146.

[20] Crafton, S. S., J. W., Rogoshchenkov, N., and Schmit, R. F., "Investigation of Passive Flow Control of Cavity Acoustics Using Dynamic Pressure-Sensitive Paint," AIAA Paper 2017-1178, 2017.
doi: 10.2514/6.2017-1178.

[21] Sakaue, H., and Sullivan, J. P., "Time Response of Anodized Aluminum Pressure-Sensitive Paint," AIAA Journal, Vol. 39, No. 10, 2001, pp. 1944–1949.
doi: 10.2514/2.1184.

[22] Sakaue, H., Kuiki, T., and Miyazaki, T., "A Temperature-Cancellation Method of Pressure-Sensitive Paint on Porous Anodic Alumina Using 1-Pyrenesulfonic Acid," Journal of Luminescence, Vol. 132, 2012, pp. 256–260.
doi: 10.1016/j.jlumin.2011.09.021.

[23] Mears, L. J., Baldwin, A., Ali, M. Y., Kumar, R., and Alvi, F. S., "Spatially Resolved Mean and Unsteady Surface Pressure in Swept SBLI Using PSP," Experiments in Fluids, Vol. 61, No. 4, 2020, pp. 1–14.
doi: 10.1007/s00348-020-2924-x.

[24] Currao, G. M. D., McQuellin, L. P., Neely, A. J., Zander, F., Buttsworth, D. R., McNamara, J. J., and Iahn, I., "Oscillating Shock Impinging on a Flat Plate at Mach 6," AIAA Paper 2019-3077, 2019.
doi: 10.2514/6.2019-3077.

[25] Varigonda, S. V., Narayanaswamy, V., and Boxx, I., "Investigations of FSI Generated by an Impinging SBLI on a Thin Panel Using Multivariate Imaging of Flow/Structural Properties," AIAA Paper 2020-3001, 2020.
doi: 10.2514/6.2020-3001.

[26] Vasconcelos, P. B., McQuellin, a. T. K., L., and Neely, A., "Hypersonic Fluid-Structure Interactions on a Compliant Clamped-Free-Clamped-Free Panel Under the Influence of Static Shock Impingement," AIAA Paper 2022-0241, 2022.
doi: 10.2514/6.2022-0241.

[27] Ahn, Y., Eitner, M. A., Musta, M. N., Sirohi, J., Clemens, N. T., and Rafati, S., "Experimental Investigation of Flow-Structure Interaction for a Compliant Panel Under a Mach 2 Compression-Ramp," AIAA Paper 2022-0293, 2022.
doi: 10.2514/6.2022-0293.

[28] Running, C. L., and Juliano, T. J., "Global Measurements of Hypersonic Shock-Wave/Boundary-Layer Interactions with Pressure-Sensitive Paint," Experiments in Fluids, Vol. 62, No. 91, 2021, pp. 1–18.
doi: 10.1007/s00348-021-03194-8.

[29] Running, C. L., and Juliano, T. J., "Global Skewness and Coherence for Hypersonic Shock-Wave/Boundary-Layer Interactions with Pressure-Sensitive Paint," Aerospace, Vol. 8, No. 123, 2021, pp. 1–14.
doi: 10.3390/aerospace8050123.

[30] Bustard, A. N., Hayashi, T., Sakaue, H., and Juliano, T. J., "Investigation of a High-Speed Duct Flow With Fast Pressure-Sensitive Paint," AIAA Paper 2022-2340, 2022.
doi: 10.2514/6.2022-2340.

[31] Gonzales, J., and Suzuki, S. H., K., "Temporally and Spatially Resolved Pressure and Temperature Maps in Hypersonic Flow," International Journal of Heat and Mass Transfer, Vol. 156, 2020, pp. 1–7.
doi: 10.1016/j.ijheatmasstransfer.2020.119782.

[32] Brouwer, K. R., Perez, R. A., Beberniss, T. J., Spottswood, S. M., Ehrhardt, D. A., and Wiebe, R., "Evaluation of Reduced-Order Aeroelastic Simulations for Shock-Dominated Flows," Journal of Fluids and Structures, Vol. 108, 2021, pp. 1–21.
doi: 10.1016/j.jfluidstructs.2021.103429.

[33] Brouwer, K. R., Perez, R. A., Beberniss, T. J., and Spottswood, S. M., "Aeroelastic Experiments and Companion Computations Assessing the Impact of Impinging Shock Sweep," AIAA Paper 2023-0945, 2023.
doi: 10.2514/6.2023-0945.

Downloaded by AFRL D'Azzo Wright-Patterson on July 13, 2023 | http://arc.aiaa.org | DOI: 10.2514/6.2023-4134

[34] Spottswood, S. M., Beberniss, T., Eason, T. G., Perez, R. A., Donbar, J. M., Ehrhardt, D. A., and Riley, Z. B., "Exploring the Response of a Thin, Flexible Panel to Shock-Turbulent Boundary-Layer Interactions," Journal of Sound and Vibration, Vol. 443, 2019, pp. 74–89.
doi: 10.1016/j.jsv.2018.11.035.

[35] Brouwer, K. R., Perez, R. A., Beberniss, T. J., Spottswood, S. M., and Ehrhardt, D. A., "Experiments on a Thin Panel Excited by Turbulent Flow and Shock/Boundary-Layer Interactions," AIAA Journal, Vol. 59, No. 7, 2021, pp. 2737–2752.
doi: 10.2514/1.J060114.

[36] Naguib, A. M., Gravante, S. P., and Wark, C. E., "Extraction of Turbulent Wall-Pressure Time-Series Using an Optimal Filtering Scheme," Experiments in Fluids, Vol. 22, 1996, pp. 14–22.
doi: 10.1007/BF01893301.

[37] Krist, S. L., Biedron, R. T., and Rumsey, C. L., "CFL3D User's Manual (Version 5.0)," NASA TM 1998-208444, 1997.

[38] Bartels, R. E., Rumsey, C. L., and Biedron, R. T., "CFL3D User's Manual - General Usage and Aeroelastic Analysis (Version 6.4)," NASA TM 2006-214301, 2006.

[39] Brouwer, K. R., Perez, R. A., Beberniss, T. J., Spottswood, S. M., Ehrhardt, D. A., and Wiebe, R., "Investigation of Aeroelastic Instabilities for a Thin Panel in Turbulent Flow," Nonlinear Dynamics, Vol. 104, 2021, pp. 3323–3346.
doi: 10.1007/s11071-021-06571-4.

[40] Sun, C., and Childs, M. E., "A Modified Wall Wake Velocity Profile for Turbulent Compressible Boundary Layers," Journal of Aircraft, Vol. 10, No. 6, 1973, pp. 381–383.
doi: 10.2514/3.44376.

[41] Musker, A. J., "Explicit Expression for the Smooth Wall Velocity Distribution in a Turbulent Boundary Layer," AIAA Journal, Vol. 17, No. 6, 1979, pp. 655–657.
doi: 10.2514/3.61193.

[42] Whitfield, D. L., and High, M. D., "Velocity-Temperature Relations in Turbulent Boundary Layers with Nonunity Prandtl Numbers," AIAA Journal, Vol. 15, No. 3, 1977, pp. 431–434.
doi: 10.2514/3.60637.

[43] Roy, C. J., and Blottner, F. G., "Review and Assessment of Turbulence Models for Hypersonic Flows," Progress in Aerospace Sciences, Vol. 42, 2006, pp. 469–530.
doi: 10.1016/j.paerosci.2006.12.002.

[44] DeBonis, J. R., Oberkampf, W. L., Wolf, R. T., Orkwis, P. D., Turner, M. G., Babinsky, H., and Benek, J. A., "Assessment of Computation Fluid Dynamics and Experimental Data for Shock Boundary-Layer Interactions," AIAA Journal, Vol. 50, No. 4, 2012, pp. 891–903.
doi: 10.2514/1.J051341.

[45] Brown, J. L., "Hypersonic Shock Wave Impingement on Turbulent Boundary Layers: Computational Analysis and Uncertainty," Journal of Spacecraft and Rockets, Vol. 50, No. 1, 2013, pp. 96–123.
doi: 10.2514/1.A32259.

[46] Wilcox, D., Turbulence Modeling for CFD, 3rd ed., DCW Industries, Inc., La Canada, California, 2006.

[47] Menter, F. R., "Two-Equation Eddy-Viscosity Turbulence Models for Engineering Applications," AIAA Journal, Vol. 32, No. 8, 1994, pp. 1598–1605.
doi: 10.2514/3.12149.

[48] Wang, B., Sandham, N. D., Hu, Z., and Liu, W., "Numerical Study of Oblique Shock-Wave/Boundary-Layer Interaction Considering Sidewall Effects," Journal of Fluid Mechanics, Vol. 767, 2015, pp. 526–561.
doi: 10.1017/jfm.2015.58.

[49] Settles, G. S., and Teng, H. Y., "Cylindrical and Conical Flow Regimes of Three-Dimensional Shock/Boundary-Layer Interactions," AIAA Journal, Vol. 22, No. 2, 1984, pp. 194–200.
doi: 10.2514/3.8367.

[50] Erengil, M. E., and Dolling, D. S., "Effects of Sweepback on Unsteady Separation in Mach 5 Compression Ramp Interactions," AIAA Journal, Vol. 31, No. 2, 1993, pp. 302–311.
doi: 10.2514/3.60176.

Downloaded by AFRL D'Azzo Wright-Patterson on July 13, 2023 | http://arc.aiaa.org | DOI: 10.2514/6.2023-4134

[51] Vanstone, L., Musta, S. S., M. N., and Clemens, N., "Experimental Study of the Mean Structure and Quasi-Conical Scaling of a Swept-Compression-Ramp Interaction at Mach 2," Journal of Fluid Mechanics, Vol. 841, 2018, pp. 1–27. doi: 10.1017/jfm.2018.8.

[52] Adler, M. C., and Gaitonde, D. V., "Flow Similarity in Strong Swept-Shock/Turbulent-Boundary-Layer Interactions," AIAA Journal, Vol. 57, No. 4, 2019, pp. 1579–1593. doi: 10.2514/1.J057534.

[53] Vanstone, L., Goller, T., Clemens, N. T., and Mears, L. J., "Separated Flow Unsteadiness in a Mach 2 Swept Compression-Ramp Interaction Using High-Speed PSP," AIAA Paper 2019-3647, 2019. doi: 10.2514/6.2019-3647.

[54] Alvi, F. S., and Settles, G. S., "Physical Model of the Swept Shock Wave/Boundary-Layer Interaction Flowfield," AIAA Journal, Vol. 30, No. 9, 1992, pp. 2252–2258. doi: 10.2514/3.11212.

[55] Schmisseur, J. D., and Dolling, D. S., "Fluctuating Wall Pressures near Separation in Highly Swept Turbulent Interactions," AIAA Journal, Vol. 32, No. 6, 1994, pp. 1151–1157. doi: 10.2514/3.12114.

[56] Arora, N., Mears, L., and Alvi, F., "Unsteady Characteristics of a Swept-Shock/Boundary-Layer Interaction at Mach 2," AIAA Journal, Vol. 57, No. 10, 2019, pp. 4548–4559. doi: 10.2514/1.J058233.

[57] Threadgill, J. A. S., and Little, J. C., "An Inviscid Analysis of Swept Oblique Shock Reflections," Journal of Fluid Mechanics, Vol. 890, No. A22, 2020, pp. 1–37. doi: 10.1017/jfm.2020.117.

[58] Padmanabhan, S., Maldonado, J. C., Threadgill, J. A., and Little, J. C., "Experimental Study of Swept Impinging Oblique Shock/Boundary-Layer Interactions," AIAA Journal, Vol. 59, No. 1, 2020, pp. 140–149. doi: 10.2514/1.J058910.

[59] Hainsworth, J., Dawson, R., and Little, J., "Experimental Study of Unswept and Swept Oblique Shock-Turbulent Boundary Layer Interactions," AIAA Paper 2014-2738, 2014. doi: 10.2514/6.2014-2738.

[60] Dawson-Ruiz, R., Pederson, C., and Little, J., "Effects of Sweep on Impinging Oblique Shock-Turbulent Boundary Layer Interaction," AIAA Paper 2015-2933, 2015. doi: 10.2514/6.2015-2933.

[61] Threadgill, J. A. S., Stab, I., Doehrmann, A., and Little, J. C., "Three-Dimensional Flow Features of Swept Impinging Oblique Shock/Boundary-Layer Interactions," AIAA Paper 2017-0759, 2017. doi: 10.2514/6.2017-0759.

[62] Doehrmann, A. C., Padmanabhan, S., Threadgill, J. A., and Little, J. C., "Effect of Sweep on the Mean and Unsteady Structures of Impinging Shock/Boundary Layer Interactions," AIAA Paper 2018-2074, 2018. doi: 10.2514/6.2018-2074.

[63] Davis, D., and Gessner, F., "Further Experiments on Supersonic Turbulent Flow Development in a Square Duct," AIAA Paper 1987-1287, 1987. doi: 10.2514/6.1987-1287.

[64] Benek, J. A., and Babinsky, H., "The Effect of Wind Tunnel Size and Shock Strength on Incident Shock Boundary Layer Interaction Experiments," AIAA Paper 2014-3336, 2014. doi: 10.2514/6.2014-3336.

[65] Pope, S. B., Turbulent Flows, Cambridge University Press, New York, NY, 2000, pp. 358–386.

[66] Reda, D. C., and Murphy, J. D., "Shock Wave/Turbulent Boundary Layer Interactions in Rectangular Channels," AIAA Journal, Vol. 11, No. 2, 1973, pp. 139–140. doi: 10.2514/3.50445.

Downloaded by AFRL D'Azzo Wright-Patterson on July 13, 2023 | http://arc.aiaa.org | DOI: 10.2514/6.2023-4134